

# Novel anisotropic teleseismic body-wave tomography code AniTomo to illuminate heterogeneous anisotropic upper mantle: Part I — Theory and inversion tuning with realistic synthetic data

Helena Munzarová<sup>1</sup>, Jaroslava Plomerová<sup>1</sup> and Eduard Kissling<sup>2</sup>

<sup>1</sup>Institute of Geophysics, Academy of Sciences, Prague, Czech Republic. E-mail: [helena@ig.cas.cz](mailto:helena@ig.cas.cz)

<sup>2</sup>Institute of Geophysics, Department of Earth Sciences, ETH Zürich, Switzerland

Accepted 2018 July 18. Received 2018 July 16; in original form 2018 February 15

## SUMMARY

Considering only isotropic wave propagation and neglecting anisotropy in teleseismic tomography studies is a simplification obviously incongruous with current understanding of the mantle–lithosphere plate dynamics. Therefore, we have developed a code for anisotropic–teleseismic tomography (AniTomo), which allows to invert relative traveltimes residuals of teleseismic *P* waves simultaneously for coupled anisotropic–isotropic *P*-wave velocity models of the upper mantle. Due to a more complex anisotropic propagation of *S* waves, the AniTomo is applicable only to *P*-wave data. Weak hexagonal anisotropy together with isotropic velocity heterogeneities are interpreted as a cause of the observed *P*-wave traveltimes residuals. Moreover, the axis of the hexagonal symmetry can be oriented freely in all directions, which represents a unique approach among recent approaches that usually incorporate only azimuthal or radial anisotropy into the body-wave tomography.

Apart from outlining the theoretical background of AniTomo, we examine various aspects coming along with anisotropic tomography such as choice of a set of initial anisotropic models and setup of parameters controlling the inversion. Synthetic testing furthermore allows investigation of the well-known trade-off between effects of *P*-wave anisotropy and lateral variations of isotropic velocity. The target synthetic models are designed to schematically represent different heterogeneous anisotropic structures of the upper mantle. Considering realistic distributions of stations and events at teleseismic distances, a separation of seismic anisotropy and isotropic velocity heterogeneities is plausible and a stable output model can be achieved within a few iterations. Careful testing of the new code on synthetics, concentrating on its functionality, strength and weaknesses, is a necessary step before AniTomo is applied to real data sets.

**Key words:** Body waves; Seismic anisotropy; Seismic tomography.

## 1 INTRODUCTION

Seismic anisotropy of the Earth's upper mantle is a key source contributing to deciphering tectonic history of the lithosphere–asthenosphere system (e.g. Babuška & Cara 1991; Šílený & Plomerová 1996; Silver 1996; Savage 1999; Park & Levin 2002; Fouch & Rondenay 2006; Mainprice 2007; Maupin & Park 2007; Long & Silver 2009; Long & Becker 2010). Smooth and long-wavelength variations of large-scale anisotropy are usually studied from propagation of surface waves (e.g. Anderson 1961; Aki & Kanamori 1963; Anderson & Dziewonski 1982; Montagner & Nataf 1986; Montagner 1994, 1998; Bruneton *et al.* 2004; Becker *et al.* 2012). Resulting shear-velocity models include azimuthal and/or radial anisotropy of the mantle prevailingly (e.g. Panning & Romanowicz 2006; Kustowski *et al.* 2008; Fichtner *et al.* 2010, 2013; Auer *et al.*

2014; French & Romanowicz 2014; Yuan *et al.* 2014; Zhu *et al.* 2014; Chang *et al.* 2015; Debayle *et al.* 2016; Ho *et al.* 2016; Nita *et al.* 2016).

In an effort to map structural variation in finer scales, one has to view the Earth with shorter wavelength optics and at different angles. Body waves, shear waves and particularly *P* waves, are sensitive to smaller-size structures due to their shorter wavelengths and broad angles of propagation in comparison with the surface waves. Thus they supply us with much more detailed information on the upper-mantle fabrics (e.g. Babuška & Plomerová 1992, 2006). However, most of standard teleseismic body-wave tomography studies neglect *P*-wave anisotropy, despite the fact that such significant simplification is incongruous with current understanding of the upper mantle–lithosphere plate dynamics. Moreover, neglecting seismic anisotropy can produce artefacts in tomographic models, both as to

amplitude and localization of heterogeneities (Sobolev *et al.* 1999; Menke 2015; Bezada *et al.* 2016).

Since the time that Backus (1965) has formulated an approximate but explicit formula for body-wave velocity of weakly anisotropic medium with a general symmetry, various methodologies incorporating anisotropy into *P*-wave traveltimes into tomography have been developed. Relatively complex and unique assumptions on anisotropy were introduced by Hirahara & Ishikawa (1984) in their pioneering traveltimes inversion for anisotropic velocity structure beneath southwest Japan. These authors determined anisotropic perturbations by a two-step inversion, in which they combined hexagonal symmetry with horizontal axis and spheroidal *P*-wave velocity surface in order to approximate orthorhombic symmetry. However, the amount of data available at that time was not sufficient to exploit advantage of the inversion for such a complex anisotropy.

Nowadays, the amount of data suitable for exploration of seismic-wave velocity anisotropy has substantially increased. Therefore, isotropic images of the Earth or those considering only azimuthal anisotropy appear incomprehensible. Such tomography models of the crust and shallow subcrustal lithosphere were calculated from traveltimes of local *P* waves for various regions, for example in Japan (Ishise & Oda 2005, 2008; Wang & Zhao 2008, 2012; Yu & Wang 2013; Ishise *et al.* 2015; Koulakov *et al.* 2015), New Zealand (Eberhart-Phillips & Henderson 2004), or Alaska (Tian & Zhao 2012). Incorporating teleseismic *P*-wave traveltimes residuals into the local data sets improved the ray coverage and depth extent of the volumes studied, for example for southeastern Tibet (Wei *et al.* 2013), the United States (Huang & Zhao 2013) or the North China Craton (Tian & Zhao 2013). Recently, new codes considering radial anisotropy of body-wave propagation have been developed, for example for the Alps (Hua *et al.* 2017) or for Japan (Wang & Zhao 2013; Huang *et al.* 2015; Gou *et al.* 2018). The radial and azimuthal anisotropy are usually modelled separately. Liu & Zhao (2017a) assume orthorhombic symmetry with a vertical symmetry axis, which leads to a simultaneous determination of azimuthal and radial anisotropy.

Another recent approach is to include not only *P* waves but also *S* waves into the anisotropic tomography. Liu & Zhao (2016, 2017b) invert *S*-wave traveltimes from local earthquakes together with relative traveltimes residuals of teleseismic *S* waves for isotropic shear-wave velocities and azimuthal anisotropy of the crust and upper mantle beneath Japan. A joint inversion of the *P*- and *S*-wave data sets results in distribution of isotropic *P*- and *S*-wave velocities and azimuthal anisotropy.

Confining orientation of the symmetry axis to horizontal (in azimuthal anisotropy) or vertical (in radial anisotropy) directions, however, does not conform to anisotropic characteristics inferred by single-station methods from teleseismic body waves, generally observed in tectonically different continental provinces (e.g. Babuška *et al.* 1984, 1993; Babuška & Plomerová 1993, 2006; Plomerová & Babuška 2010; Plomerová *et al.* 2011, 2012). These authors demonstrate dependence of SKS-wave splitting parameters and *P*-wave traveltimes residuals on direction of wave propagations, taking into account both azimuth and incidence angles. Such characteristics with a general  $2\pi$  periodicity imply a need to treat anisotropy in 3-D. This allows us to evaluate fabrics of the upper mantle, in particular within the mantle lithosphere, without any limiting assumption on orientation of symmetry axes. Self-consistent anisotropic models of continental mantle lithosphere usually document (e.g. Plomerová *et al.* 2011) that derived symmetry axes of the anisotropic domains are oriented generally in 3-D, that is inclined from horizontal.

In this methodological paper, we present a novel and unique tomographic code called AniTomo that allows us to invert relative traveltimes residuals of teleseismic *P* waves for 3-D distribution of both isotropic and anisotropic *P*-wave velocities in the upper mantle. This code represents a step further from modelling 3-D self-consistent homogeneously anisotropic blocks of mantle lithosphere (e.g. Babuška *et al.* 1993; Šílený & Plomerová 1996; Vecsey *et al.* 2007), towards modelling the upper mantle with anisotropy arbitrarily varying in 3-D. The AniTomo code for coupled anisotropic-isotropic tomography assumes weak anisotropy with hexagonal symmetry typical for upper mantle, either with high-velocity *a*-axis or low-velocity *b*-axis, oriented generally in 3-D. An important option of the code is the possibility to decide whether anisotropic, or isotropic, or both inversions will be performed in each node. Of course, ray coverage controls in which part of a model the coupled anisotropic-isotropic inversion is feasible. Apart from deriving the equations for this specific type of tomography, we document, with a series of synthetic tests, effects of the inversion setup on the results. The tests mimic realistic tomographic inversions in terms of target synthetic model representing anisotropic structures of the upper mantle, particularly the anisotropic domain-like structure of the mantle lithosphere, and also in terms of amount and incidence angles of teleseismic *P*-wave data. On the other hand, we keep the azimuthal coverage uniform not to bias the tests of, for example regularization of the inversion, by any directional asymmetry. Testing carefully the new code on synthetics, concentrating on its functionality, strengths and weaknesses, represents a necessary step before an application of AniTomo to real data sets. First, we apply the new AniTomo code on data from northern Fennoscandia (Munzarová *et al.* 2018, revision submitted), where also real non-uniform ray distributions are tested.

## 2 THEORY

We aim at modelling anisotropic upper-mantle structures with the use of teleseismic *P*-wave tomography. The crucial part of the theory is derivation of an explicit formula for *P*-wave velocities in weakly anisotropic medium with hexagonal-symmetry axis oriented generally in 3-D. Then, linearization of the relation between data (traveltimes residuals) and model parameters describing the anisotropic medium is straightforward.

### 2.1 *P*-wave velocity in weakly anisotropic medium with hexagonal-symmetry axis generally oriented in 3-D

Backus (1965) applied first-order expansion of Christoffel equation for propagation of plane waves in homogeneous anisotropic elastic medium and he found an approximate but explicit formula for body-wave velocity *v* in weakly anisotropic medium with a general symmetry

$$v = c + \frac{B^{(1)}}{2c}, \quad (1)$$

where *c* is wave velocity in isotropic medium and  $B^{(1)}$  is the 1st-order perturbation of the non-degenerated eigenvalue of Christoffel tensor. Particularly for *P* waves,  $B^{(1)}$  can be expressed as

$$B^{(1)} = \gamma_{ijkl} n_i n_j n_k n_l, \quad (2)$$

where  $\gamma_{ijkl}$  are small variations of isotropic density-normalized elastic coefficients adjusting for the weak anisotropy. Vector **n** represents the *P*-wave propagation direction.

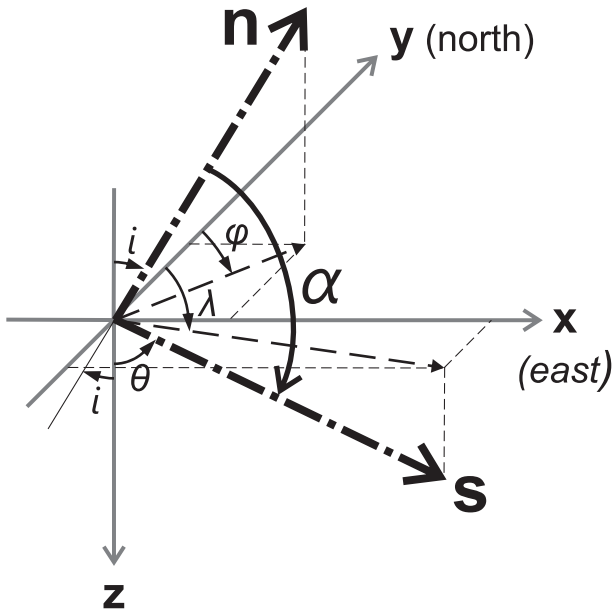


**Figure 1.** Definition of the Cartesian coordinate system used in AniTomo. Angles  $\lambda$  and  $\theta$  label azimuth and inclination of the hexagonal-symmetry axis (unit vector  $s$ ), respectively. Wave-propagation direction is represented by unit vector  $n$ . Angles  $\phi$  and  $i$  mark backazimuth and angle of propagation of the wave, respectively.  $\alpha$  is angle between the symmetry axis and the wave-propagation direction.

We present a detailed description of implementing hexagonal symmetry into eq. (2) and derivation of anisotropic velocity (eq. 1) in Appendix A. Then, the velocity for this specific symmetry is

$$v = \bar{v} \left( 1 + \frac{k}{2} \cos 2\alpha \right), \quad (3)$$

where  $\bar{v}$  is isotropic component of anisotropic velocity,  $k$  is strength of anisotropy and  $\alpha$  is an angle between the symmetry axis and wave-propagation direction (Fig. 1).

As AniTomo employs only  $P$  wave and no  $S$  wave traveltimes, we cannot recover the five elastic coefficients of the anisotropy with assumed hexagonal symmetry individually, but only their combinations. We translate these combinations into isotropic component of velocity  $\bar{v}$  and strength of anisotropy  $k$  (Appendix A), which we express as

$$\bar{v}^2 = \frac{1}{8\rho} [3(A+C) + 2(F+2L)], \quad (4)$$

$$k = \frac{4(C-A)}{3(A+C) + 2(F+2L)}, \quad (5)$$

where  $\rho$  is density. Positive values of strength of anisotropy correspond to hexagonal symmetry with axis  $a$  in direction of high velocity (call high-velocity  $a$ -axis), perpendicular to low-velocity plane ( $b,c$ ), and vice versa—negative values correspond to hexagonal symmetry with axis  $b$  in direction of low velocity (call low-velocity  $b$ -axis), perpendicular to high-velocity plane ( $a,c$ ) (Fig. S1).

Fig. S1(b) documents that the cosine function (eq. 3) is a sufficient approximation of  $P$ -wave velocities in the upper mantle in the case of weakly anisotropic medium with hexagonal symmetry. The maximum difference between the  $P$ -wave velocities calculated according to approximate eq. (3) and evaluated as the exact solution

of the Christoffel equation is only  $\sim 0.5$  per cent for an anisotropic upper-mantle approximated by peridotite aggregate (Ben Ismail & Mainprice 1998; Babuška & Plomerová 2006).

In order to transform angle  $\alpha$  into ray-parameter coordinate system, we define orientation of the symmetry axis by unit vector  $s$  and propagation direction of the wave by unit vector  $n$  (Fig. 1) as

$$s = (\sin \theta \sin \lambda, \sin \theta \cos \lambda, \cos \theta), \quad (6)$$

where  $\lambda$  and  $\theta$  are azimuth and inclination (measured upward from vertical) of the symmetry axis and

$$n = (-\sin i \sin \phi, -\sin i \cos \phi, -\cos i), \quad (7)$$

where  $\phi$  and  $i$  are backazimuth and incidence angle of the wave propagation. After substituting  $\cos 2\alpha = 2\cos^2 \alpha - 1$  and  $\cos \alpha = \mathbf{n} \cdot \mathbf{s}$  in eq. (3), the  $P$ -wave velocity in weakly anisotropic medium with hexagonal symmetry and a general orientation in 3-D can be expressed as

$$v = \bar{v} \left\{ 1 + k \left[ (\sin i \sin \theta \cos(\phi - \lambda) + \cos i \cos \theta)^2 - \frac{1}{2} \right] \right\}. \quad (8)$$

This equation relates anisotropic velocity  $v$  of a  $P$ -wave propagating in direction given by angles  $\phi$  and  $i$  with isotropic component  $\bar{v}$  of anisotropic velocity and directionally variable velocity perturbation, that is the term with strength of anisotropy  $k$ .

## 2.2 System of linearized equations

Similarly to the isotropic tomography, AniTomo needs a linearized relation between traveltime residual  $\Delta t$  and model parameters, that is perturbations of the parameters describing the medium  $\Delta \bar{v}$ ,  $\Delta k$ ,  $\Delta \lambda$  and  $\Delta \theta$ ,

$$\begin{aligned} \Delta t = \sum_j \left( \frac{\partial t}{\partial \bar{v}} \right)_j \Delta \bar{v}_j + \sum_j \left( \frac{\partial t}{\partial k} \right)_j \Delta k_j + \sum_j \left( \frac{\partial t}{\partial \lambda} \right)_j \Delta \lambda_j \\ + \sum_j \left( \frac{\partial t}{\partial \theta} \right)_j \Delta \theta_j, \end{aligned} \quad (9)$$

where index  $j$  denotes contribution to the traveltime residual from the  $j$ th ray segment. The traveltime  $t$  of a  $P$  wave in the anisotropic medium is

$$t = \frac{s}{v(\bar{v}, k, \lambda, \theta)}, \quad (10)$$

where  $v(\bar{v}, k, \lambda, \theta)$  stands for the anisotropic velocity (eq. 8). Partial derivatives of the traveltime with respect to the anisotropic parameters in eq. (9) are then

$$\frac{\partial t}{\partial \bar{v}} = -\frac{s}{v_0 \cdot \bar{v}_0}, \quad (11)$$

$$\frac{\partial t}{\partial k} = -\frac{s}{v_0} \cdot \left[ (\sin i \sin \theta \cos(\phi - \lambda_0) + \cos i \cos \theta)^2 - \frac{1}{2} \right], \quad (12)$$

$$\begin{aligned} \frac{\partial t}{\partial \lambda} = -\frac{s}{v_0} \cdot 2k_0 (\sin i \sin \theta \cos(\phi - \lambda_0) + \cos i \cos \theta) \\ \times \sin i \sin \theta \sin(\phi - \lambda_0), \end{aligned} \quad (13)$$

$$\begin{aligned} \frac{\partial t}{\partial \theta} = -\frac{s}{v_0} \cdot 2k_0 (\sin i \sin \theta \cos(\phi - \lambda_0) + \cos i \cos \theta) \\ \times (\sin i \cos \theta \cos(\phi - \lambda_0) - \cos i \sin \theta). \end{aligned} \quad (14)$$

As the partial derivatives depend on anisotropic parameters, the problem is still non-linear. Thus, we fix the anisotropic parameters in eqs (11)–(14) to the reference values (marked with index 0) and solve the problem iteratively. The reference values come from the initial model during the first iteration and from the model resulting after the  $(n-1)$ th iteration during the  $n$ th iteration.

Eq. (9) established for individual station-event  $P$  wave traveltimes residuals form a system of linearized equations that is solved with the damped least-square method (Menke 1984). During the  $n$ th iteration, we obtain vector of model parameters updating the solution from the previous iterations at all the grid nodes

$$\mathbf{m}^{(n)} = (\mathbf{A}^T \mathbf{W}_D \mathbf{A} + \epsilon \mathbf{W}_M)^{-1} \mathbf{A}^T \mathbf{W}_D \mathbf{d}^{(n-1)}. \quad (15)$$

Vector  $\mathbf{d}^{(n-1)}$  contains traveltimes evaluated for the reference model equal to the solution from the  $(n-1)$ th iteration. The partial derivatives (eqs 11–14) are stored in matrix  $\mathbf{A}$ . Errors of arrival-time measurements can be reflected in weighting matrix  $\mathbf{W}_D$ . Stabilization of the ill-posed problem can be achieved through damping factor  $\epsilon^2$  and smoothing matrix  $\mathbf{W}_M$ . Damping factor controls prediction error versus solution length (Menke 1984).

To assess reliability of the model parameters for a given ray distribution and inversion setup, we evaluate an approximation of the resolution matrix as

$$\mathbf{R} = (\mathbf{A}^T \mathbf{W}_D \mathbf{A} + \epsilon^2 \mathbf{W}_M)^{-1} \mathbf{A}^T \mathbf{W}_D \mathbf{A}. \quad (16)$$

Diagonal elements of resolution matrix (RDE) represent how well an estimate of model parameters can fit the true solution based on the ray geometry within the parametrization cells (Menke 1984). We parametrize the volume studied by an orthogonal grid of nodes. Off the nodes, the isotropic component of velocity is determined by a linear interpolation and strength of anisotropy and symmetry-axis orientation are assumed constant in each cell surrounding the grid node.

### 3 ANITOMO-TOMOGRAPHY CODE WITH IMPLEMENTED 3-D ANISOTROPY

The developed coupled anisotropic-isotropic tomography code (AniTomo) has been created as a modification of widely used code Telinv for high-resolution regional isotropic tomography of the upper mantle from residuals of traveltimes of teleseismic body waves. Telinv is a Fortran code originally developed by J. Taylor, E. Kissling, U. Achauer, C. M. Weiland and L. Steck. It has been used and modified by many authors (e.g. Weiland *et al.* 1995; Arlitt *et al.* 1999; Lippitsch *et al.* 2003; Sandoval *et al.* 2004; Shomali *et al.* 2006; Eken *et al.* 2007; Karousová *et al.* 2012, 2013; Karousová 2013; Plomerová *et al.* 2016; Silvennoinen *et al.* 2016; Chyba *et al.* 2017). Actual updated version of the Telinv code can be downloaded from <http://www.ig.cas.cz/en/research-teaching/software-are-download/>.

In order to step from isotropic (Telinv) to  $P$ -wave anisotropic tomography (AniTomo), we have implemented equations derived in Section 2 into the original code. The coupled anisotropic-isotropic code AniTomo allows to run both isotropic and/or fully 3-D anisotropic inversions. We have kept the overall framework and the subroutines solving the individual steps especially of linear algebra as they were in Telinv. This chapter focuses on key attributes of the AniTomo anisotropic-tomography code. For more information on specific procedures related already to Telinv, we refer the reader

to the publications dedicated to isotropic tomography mentioned in above paragraph.

AniTomo is a new and unique code for regional traveltimes anisotropic tomography of the upper mantle. Traveltimes residuals of teleseismic  $P$  waves are inverted for anisotropy velocity model described by parameters of weak anisotropy with hexagonal symmetry. These model parameters are perturbations of isotropic component of anisotropic velocity, strength of anisotropy and general orientation of the symmetry axis in 3-D defined by its inclination and azimuth. Directionally dependent velocities of wave propagation are evaluated according to eq. (8) whenever it is required, for example during ray tracing or calculation of the partial derivatives of traveltimes. Eq. (8) is valid only for  $P$  waves in weakly anisotropic media with hexagonal symmetry and axes oriented generally in 3-D. Thus AniTomo can not be used for  $S$  waves, for which anisotropic propagation is more complex.

The inversion starts from an anisotropic initial model, in which starting parameters have to be specified in each parametrization node. Final model is obtained after iterative updating of the initial model. We can either start the inversion from a homogeneous very weak ( $\sim 1$  per cent) anisotropic model or involve some a-priori information on anisotropy, for example from previous studies, into the initial model. Sections 4 and 5 survey the choice of initial model.

To adapt the original isotropic code for its anisotropic version, we enlarge number of unknown parameters, because we iteratively search for up to four model parameters at each node of a 3-D orthogonal grid. Thus, total number of model parameters is four times larger compared to the isotropic tomography. Due to the increased complexity, good ray coverage of the model in terms of number and directional distribution of the rays is crucial for a reliable inversion. The code is written in such a way that we can fix any parameter when it is not well determined. Thus, we can limit anisotropic inversion only to a well-resolved part of the volume studied and run isotropic inversion in the remaining volume simultaneously. Purely isotropic inversion is also possible with AniTomo.

Further step, adapting the inversion for anisotropy, was an extension of matrix  $\mathbf{A}$  (eq. 15) to include partial derivatives of traveltimes with respect to each of the four anisotropic parameters (eqs 11–14). Matrix  $\mathbf{A}$  is now a block matrix containing up to four blocks. The size of the blocks depends on number of unknowns for each of the four anisotropic parameters. Smoothing matrix  $\mathbf{W}_M$  (eq. 15), which enables horizontal Laplacian smoothing of any of the four types of model parameters, is of the same block structure. Any of the blocks is set to identity when the respective smoothing option is switched off. Damping factor  $\epsilon^2$  is assigned separately to each type of the model parameters (see Section 4). The inverse of matrix in eq. (15) is computed by truncated singular value decomposition.

Resolution matrix (16) is also made up of one block for each of the four types of model parameters. As the resolution matrix contains partial derivatives, resolvability of azimuth and inclination of the symmetry axis directly depends on strength of anisotropy (eqs 13–14). Thus, in the case of relatively low strength of anisotropy we obtain a very low RDE for axis orientation despite a very good ray coverage. It simply means that for a too low value of anisotropy, orientation of the symmetry axis is not resolved reliably (see Section 4.4).

Attention should be paid to quality of directional coverage of the volume studied by rays. In order to express 3-D distribution of the rays within the parametrization cells, we implemented in AniTomo calculations of ray density tensor (Kissling 1988; Sandoval 2002; Sandoval *et al.* 2004). Detailed theoretical background of evaluation of the ray density tensors (RDT) is presented in Appendix B.

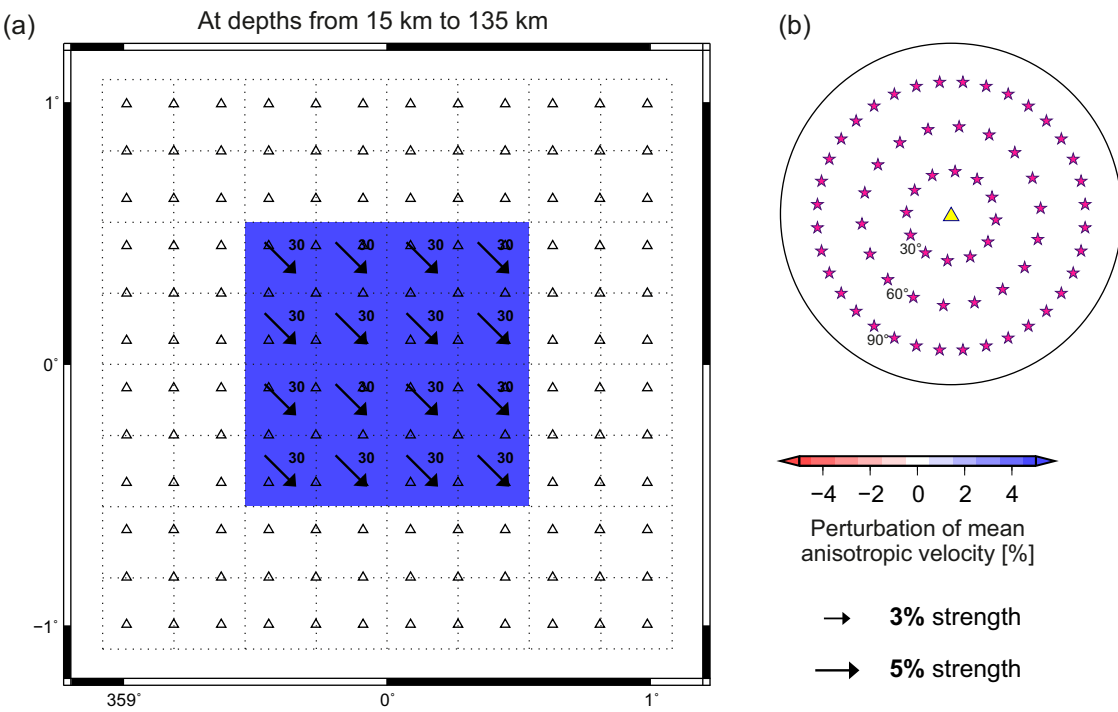


**Figure 2.** Model of high-velocity heterogeneity with dipping anisotropy designed for synthetic tests of influence of damping and initial model on the solution (a). The velocity perturbation of the heterogeneity is 5 per cent relative to IASP'91. The strength of anisotropy with dipping symmetry axis towards southeast is also 5 per cent. The arrows indicate strength of anisotropy and azimuth of orientation of the symmetry axis at the parametrization nodes. In general, we plot the arrows only for anisotropy stronger than 1 per cent. Axis inclination measured upward from vertical is marked with a number next to the arrow. A case of a low-velocity symmetry axis would be marked with 'b', otherwise the axis is high-velocity. The horizontal distribution of pparametrization cells, each of which is centred around an inversion node, is marked with dotted lines. Stations located at the surface with 20 km spacing are represented by triangles. Locations of events regularly distributed in teleseismic distances are in (b).

#### 4 SYNTHETIC TESTS I—EFFECTS OF DAMPING AND INITIAL MODEL SETUP ON THE FINAL OUTPUT MODEL

Power of synthetic tests results from a possibility to compare the final output model with the original input model. Thus, one can directly see the impact of a specific inversion setup on the solution, unlike in a real case. Synthetic tests are useful to become familiar with any new code, to explore its strengths and weaknesses before applying it routinely as well as to establish a proper model-volume parametrization, find optimum control parameters and explore capability of the given ray coverage to resolve the model parameters, always when a new data set is to be processed. In the case of the new anisotropic code AniTomo, it is essential to examine various aspects of this unique approach. In this chapter, we demonstrate how the choice of damping (eq. 15) and of the initial anisotropic model influence the resulting model. The synthetic model designed for this methodological purpose is very simple. Tests with a more complex synthetic structure are in Section 5. Effects on non-uniform ray distribution in real data are tested in the accompanying paper (Munzarová *et al.* 2018, revision submitted).

##### 4.1 Setup of methodological synthetic experiments

In order to mimic a setup of a regional teleseismic tomography of the Earth's upper mantle, particularly the continental mantle lithosphere, we consider a volume of 240 km × 240 km × 120 km with a synthetic anisotropic heterogeneity of 120 km × 120 km × 120 km in the middle (Fig. 2). The heterogeneity is characterized

by an isotropic velocity component that is 5 per cent higher than the IASP'91 reference model (Kennett & Engdahl 1991). Furthermore, we assign anisotropy of 5 per cent strength to the synthetic heterogeneity. The anisotropy has hexagonal symmetry with high-velocity *a*-axis. We note that the type of symmetry axis is determined in AniTomo only by the sign of strength of anisotropy, that is by positive strength for high-velocity *a*-axis and by negative sign for low-velocity *b*-axis (Section 2). The inversion, in principle, does not favour any type of the symmetry. Orientation of the symmetry axis of the synthetic anisotropic heterogeneity is defined by azimuth of 135° and inclination of 30°, measured upward from vertical.

We parametrize the volume studied by an orthogonal 3-D grid of  $8 \times 8 \times 4$  nodes, in which the model parameters are searched. Grid spacing is 30 km both horizontally and vertically. Synthetic set of 9504 rays corresponds to *P* waves propagating from 66 equally distributed teleseismic events to 144 stations located at the surface above the volume studied (Fig. 2b). Input data set for the synthetic tests of AniTomo consists of traveltimes residuals calculated as differences between the traveltimes of *P* waves passing through the synthetic structure described above and the traveltimes calculated for the IASP'91 reference model. Gaussian errors with standard deviation of 0.05 s are added to the calculated traveltimes mimicking the observation errors. Smoothing of the model parameters is switched off. All the inversions run for eight iterations in order to evaluate both the stability of the inversion and the character of convergence of the model parameters in dependence on number of iterations. In the following parts, we test influence of damping and initial anisotropic model on inversion stability and development of model parameters.

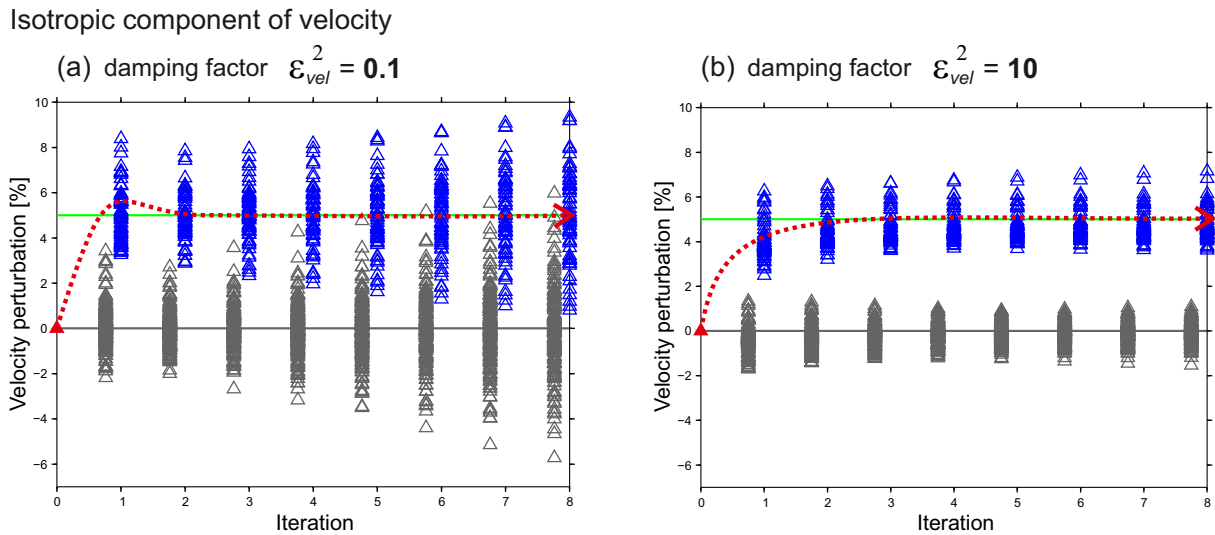


**Figure 3.** Perturbations of isotropic components of velocity for damping factor of 0.1 (a) and 10 (b). To show evolution of the model parameters with increasing iteration number, we plot them for all the nodes and all the iterations in one graph. The model parameters of the nodes with the high-velocity anisotropic heterogeneity in the synthetic model (Fig. 2) are distinguished with blue colour from the model parameters of the surrounding nodes (grey). Green and grey lines indicate the target model values of the nodes with and without the synthetic heterogeneity, respectively. Red triangle marks the initial value assigned to all the nodes before the inversion. Red dotted curve tracks the overall trend of the model parameters belonging to the nodes with the synthetic heterogeneity. The damping factors strongly influence the rate of convergence and the scattering in the results for all model parameters. See Fig. S2(b) for an example with a higher value of damping.

#### 4.2 Effect of damping factor on the solution

Damping is a regularization parameter that helps to stabilize inversion of underdetermined problems by minimizing a combination of prediction error and solution length (eq. 15; Menke 1984). The choice of damping factor affects rate of convergence of the model parameters, their overall amplitude and scatter in dependence on number of iterations. A well-selected damping factor suppresses small or even single-cell anomalies, coming mostly from data errors, or large perturbations in less resolved nodes. Different values of damping have to be assigned to each of the four types of model parameters, which are isotropic component of anisotropic velocity, strength of anisotropy and azimuth and inclination for orientation of the symmetry axis. Therefore, the damping factors defined as follows:

$$[\varepsilon_{vel}^2] = \left[ \frac{\Delta t^2}{\Delta \bar{v}^2} \right] = \frac{s^4}{km^2}, \quad (17)$$

$$[\varepsilon_{stren}^2] = \left[ \frac{\Delta t^2}{\Delta k^2} \right] = s^2, \quad (18)$$

$$[\varepsilon_{azim}^2] = \left[ \frac{\Delta t^2}{\Delta \lambda^2} \right] = \frac{s^2}{rad^2}, \quad (19)$$

$$[\varepsilon_{incl}^2] = \left[ \frac{\Delta t^2}{\Delta \theta^2} \right] = \frac{s^2}{rad^2}, \quad (20)$$

have different physical meaning. Though it is necessary to treat each damping factor as an individual quantity, they are related among themselves. The proper values differ for individual data sets and inversion settings.

The most common way of displaying effects of different inversion setups, apart from plotting the output model itself, is to draw trade-off curves, that is model- and data-variance pairs. In order to get a

more detailed insight into the influence of a given inversion setup, we investigate evolution of the model parameters with increasing number of iterations. In such a way, we can examine how fast and how precisely the output model parameters reach the correct values in dependence on different factors of damping (Figs 3–5 and Fig. S2). During these synthetic tests, we always change only one of the four damping factors, while the three others as well as other settings remain fixed. Below, we evaluate effects of intensity of damping on the convergence rates and scatter of isotropic component of velocity, anisotropy strength and axis inclination for Synthetic model I (parameters see above).

Quite a wide range of damping factors leads to a stable inversion for perturbations of isotropic component of anisotropic velocity. The retrieved model velocities converge fast to the correct values of the target model (Fig. 3). On the other hand, different values of damping distinctly affect scatter of the perturbations. The scatter around the target velocities increases with increasing number of iterations of the inversion with low damping of 0.1, while the model velocities for damping of 10, chosen as the appropriate one, form a narrow band of a constant scatter around the target value. Damping of 100 is, on the contrary, too high and it evidently slows down the convergence of the isotropic-velocity perturbations (Fig. S2b). Fig. 4 and Fig. S2(d) show the same kind of plots for low, medium and high damping of strength of anisotropy with factors of 0.1, 100 and 1000. Damping of 100 significantly reduces the scattering of anisotropy strength but it also slows down the convergence.

In the case of azimuth and inclination, which define the orientation of the symmetry axis, well-tuned damping factors are essential for stability of the inversion because of non-linearity between the angles and the anisotropic velocity (eq. 8). Damping controls step length for each iteration of the model parameters. Linearization requires the step length to be short enough to assure relatively slow changes of azimuths and inclinations towards the correct solution. In the case of low damping factor (Fig. 5a), the model inclinations

## Strength of anisotropy

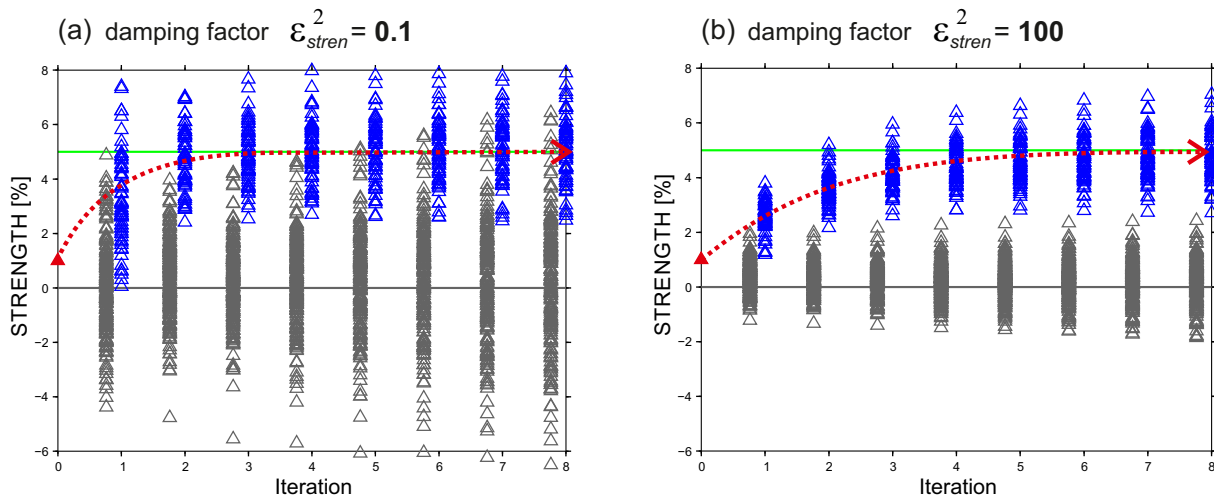


**Figure 4.** Resulting model parameters corresponding to strength of anisotropy after individual iterations for damping factor of 0.1 (a) and 100 (b). See Fig. S2(d) for an example with a higher value of damping. See also caption of Fig. 3.

## Inclination of symmetry axis

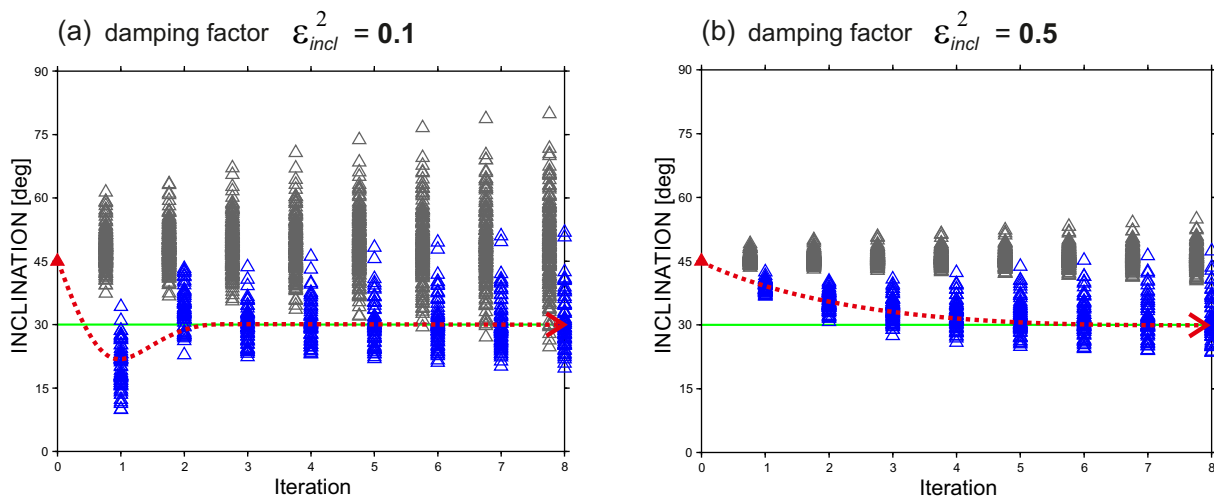


**Figure 5.** Resulting model parameters corresponding to inclination of symmetry axis after individual iterations for damping factor of 0.1 (a) and 0.5 (b). See Fig. S2(f) for an example with a higher value of damping. See also caption of Fig. 3.

overshoot the correct values after the first iteration. However, despite that the inclinations converge fast to the target values and the inversion remains stable. On the contrary, the higher damping factor results in a slow steady convergence of the model inclinations (Fig. 5b).

According to rate of convergence and scatter of the model parameters we choose 1, 100, 0.1 and 0.5 damping for isotropic component of velocity, strength of anisotropy and azimuth and inclination of the symmetry axis, respectively. This combination of damping factors leads to fluently converging model parameters and it minimizes their scatter. In this series of synthetic tests, we have demonstrated how damping of anisotropic inversion affects the resulting model. Well-tuned factors of damping of all the model parameters are essential for a stable inversion. On the other hand, testing different

inversion settings is appropriate not only for anisotropic tomography but generally.

### 4.3 Effect of initial model setup on the solution

Another aspect of anisotropic inversion, which is relevant to be tested on synthetics, is setting up an initial anisotropic model. The inversion should start from a model that is relatively close to the target one to satisfy conditions of linearization of the traveltime equation (eq. 9). This is a well-known assumption also from isotropic tomography, which is generally fulfilled in the upper mantle for standard reference earth models, for example IASP'91 (Kennett & Engdahl 1991) or ak135 (Kennett *et al.* 1995; Montagner & Kennett 1996), or a minimum 1-D model in local earthquake tomography (e.g. Kissling 1988; Spakman *et al.* 1993; Kissling & Spakman

1996). Nevertheless, what does it mean for anisotropic tomography and what limitations does it introduce? Attention must be paid particularly to orientation of the symmetry axis, whose the relation to anisotropic velocity (eq. 8) is not linear. In the following tests, we prescribe different initial models containing non-zero homogeneous anisotropy in all the grid nodes, where the model parameters are searched, to investigate effect of the initial setup on the output model.

Fig. 6 shows evolution of model parameters in relation to number of iterations for initial models with differently oriented axis of hexagonal symmetry. In the first model we assume initial azimuth of 45° and in the second one the initial azimuth is 180°, whereas the target azimuth is 135° at the nodes with the synthetic anisotropic heterogeneity. Despite the 90° difference between the first initial and the target azimuths, most of the model azimuths tend to approach the target value (blue triangles in Fig. 6a). There is no surprise that the iterative model azimuths converge better and faster in the case of initial model with azimuth of 180°, which is closer to the target value of 135° (Fig. 6b). We can conclude that the closer the initial model parameters are to the target ones, the faster the iterative model parameters converge to the correct values. It is evident that the choice of the initial orientation of the symmetry axis influences the resulting model. Therefore, we advocate necessity of an appropriate and systematic scanning of the volume with a set of initial orientations. We discuss that in Sections 5.1 and 5.2.

Fig. 7 shows influence of the initial value of strength of anisotropy on the results. Starting the inversion with 5 per cent anisotropy, which might be considered as an approximation of peridotitic upper mantle, it is difficult to eliminate anisotropy artificially assigned to the boundary nodes of Synthetic model I, where only isotropic velocities were prescribed (a). On the contrary, a better recovery of both the isotropic and anisotropic parts of the model is obvious in the case of iterative inversions initiated from weak anisotropy strength of 1 per cent (b). However, we avoid starting the inversion with anisotropy strength set to 0 per cent, because it is equivalent to fixing the azimuth and inclination of the symmetry axis during the first iteration (eqs 13–14). These tests have shown that a very weak initial strength of anisotropy does not impose artificial anisotropy into the isotropic part of the model and that it enables a fluent convergence of the iterative strength parameters within the anisotropic part of the model.

#### 4.4 Resulting model of the methodological synthetic experiment

Finally, we present the model (Fig. 8) that comes out from the 4<sup>th</sup> iteration of the inversion with well-tuned damping factors (Section 4.2) and with the initial model as follows: isotropic velocity equal to the IASP'91 velocities, strength of anisotropy of 1 per cent, and azimuth and inclination of the symmetry axis of 180° and 45°, respectively. 3-D shape of the heterogeneity is perfectly restored for all anisotropic parameters. No lateral deformation of the heterogeneity occurs. An area of negative-velocity perturbations with low amplitudes, particularly at 30 km depth, neighbours the high-velocity heterogeneity in the centre. It might be due to the general incapability of teleseismic tomography to recover the absolute velocities. The reduction of data variance is 98 per cent and the remaining traveltimes residuals are at the level of noise of 0.05 s.

As a matter of interest, we plot diagonal elements resolution matrix (RDE; eq. 16) for the model investigated in this section in

Fig. S3. While resolution of the isotropic component of velocity and strength of anisotropy is perfect everywhere, the image of RDE for azimuth and inclination of symmetry axis follows shape of the anisotropic heterogeneity. RDE are high enough in the central part, where the anisotropic heterogeneity is in the input model, but outside of the anisotropic region, the RDE are low. As there is no anisotropy in this part of the model, the axis might turn arbitrarily there. This is in agreement with eqs (13) and (14).

## 5 SYNTHETIC TESTS II—ASSESSING POTENTIAL TRADE-OFF BETWEEN ANISOTROPY AND ISOTROPIC HETEROGENEITY

### 5.1 Setup of the synthetic experiment representing domain-like structure of continental mantle lithosphere

Series of synthetic inversions presented in this chapter focus on setting initial models for anisotropic tomography of the mantle lithosphere and the sublithospheric mantle. The Synthetic model II, mimicking a domain-like structure of continental mantle lithosphere, occupies 240 km × 240 km × 240 km, that is it is twice as deep as the Synthetic model I in Section 4. We enlarge the thickness of the model, in order to examine depth resolution of the method. We keep spacing between the nodes at 30 km both horizontally and vertically, resulting in 8 × 8 × 8 grid nodes, in which the unknown model parameters are searched. We use the same synthetic quasi-equal distribution of 9504 teleseismic *P* waves as in Section 4. The Synthetic model II consists of three blocks, two of which are anisotropic (northwestern and southern) and one (northeastern) is purely isotropic. The blocks differ in their shapes as well. All the three blocks extend from 45 km down to 135 km and they are characterized by different isotropic components of anisotropic velocity (Fig. 9 and Table 1). The anisotropic blocks possess 5 per cent anisotropy with different orientations of the symmetry axes. The isotropic velocities are non-perturbed above and below the three blocks. Such a synthetic model of sharply bounded anisotropic blocks is motivated by a concept of continental mantle lithosphere being formed as an assemblage of lithospheric domains, preserving their mean velocities and fossil fabrics (e.g. Plomerová & Babuška 2010).

During the inversion, damping factors are the same as those adopted as optimum for the methodological synthetic test I (Section 4.4), because we keep the parametrization grid, the ray coverage and the synthetic-data error. We demonstrated in Section 4.3 that the output model depends on the angular deviation between the orientation of symmetry axes of the initial and the searched model due to the non-linear relation between anisotropic velocity and orientation of the symmetry axis (eq. 8). Therefore, we keep the IASP'91 velocities and strength of anisotropy of 1 per cent in the initial model and we repeat the inversion for regularly changing setups of initial azimuths and inclinations. We invert twelve times with all combinations of initial azimuths (0°, 90°, 180° and 270°) and inclinations (10°—subvertical axis, 45°—dipping axis and 80°—subhorizontal axis) in order to systematically cover the range of initial orientations of the hexagonal-symmetry axis. By this procedure we minimize a danger that the resulting model will be affected by the initial setup of anisotropy orientation.

## Azimuth of symmetry axis

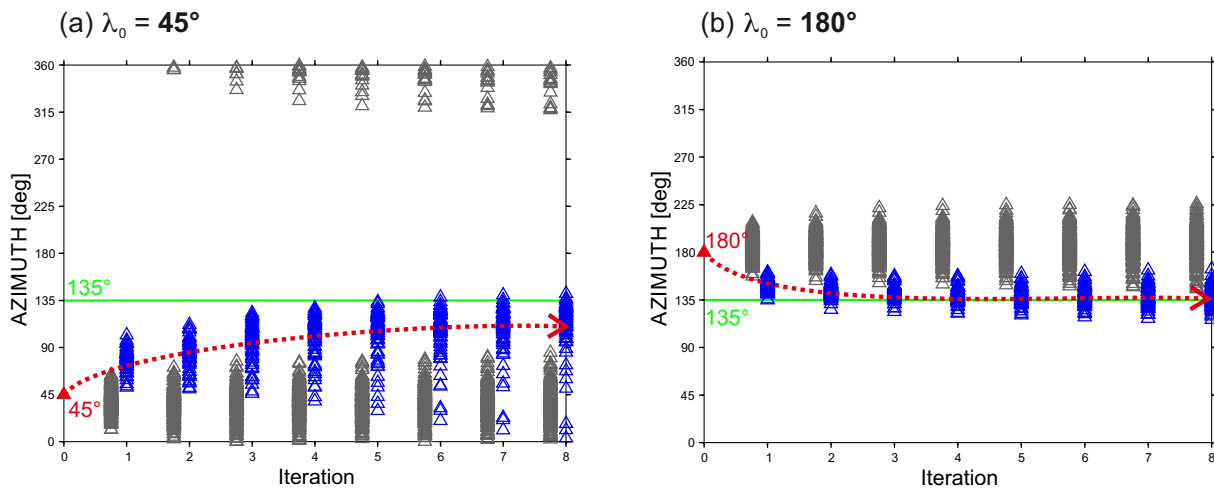


**Figure 6.** Resulting model parameters corresponding to azimuth of the symmetry axis after individual iterations for the initial values of  $45^\circ$  (a) and  $180^\circ$  (b). See also caption of Fig. 3.

## Strength of anisotropy

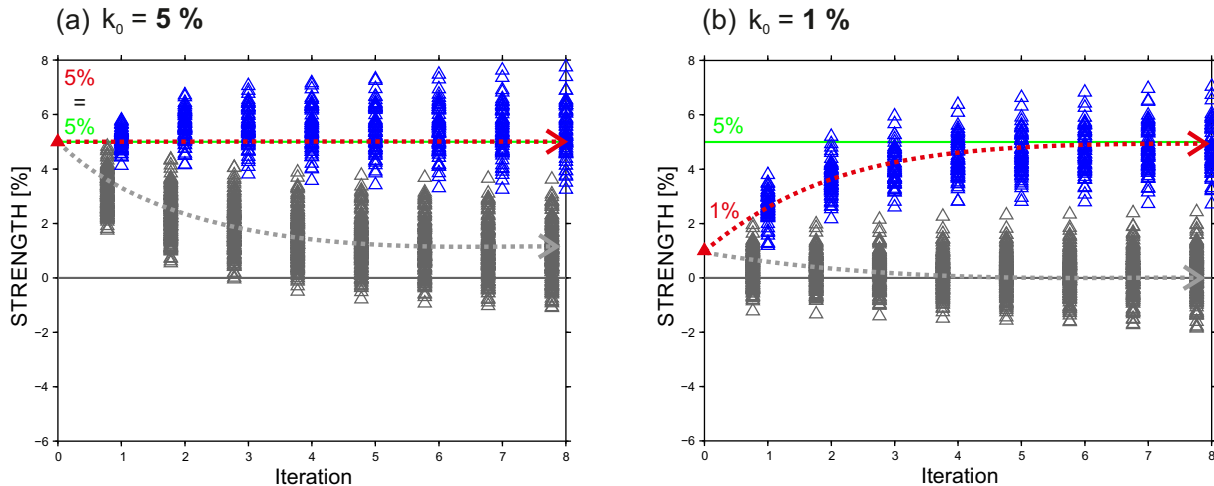


**Figure 7.** Resulting model parameters corresponding to strength of anisotropy after individual iterations for the initial values of 5 per cent (a) and 1 per cent (b). See also caption of Fig. 3.

## 5.2 Resulting model of the synthetic experiment representing domain-like structure of continental mantle lithosphere

Fig. 10 shows output model parameters at depth of 90 km from three types of inversions according to initial inclination: with initial symmetry axis inclined at  $45^\circ$  successively at azimuths of  $0^\circ$  (a),  $90^\circ$  (b),  $180^\circ$  (c) and  $270^\circ$  (d), with a subvertical axis orientation of  $10^\circ$  inclination and azimuth of  $0^\circ$  (e) and a subhorizontal orientation of  $80^\circ$  inclination and azimuth of  $90^\circ$  (f). For results in other depths we refer to Fig. S4. Anisotropy in the northwestern block characterized by axis inclining  $50^\circ$  from vertical in azimuth of  $120^\circ$  (Fig. 9 and Table 1) is well recovered for the initial models with inclined initial axis in azimuth of  $90^\circ$  (Fig. 10b) or  $180^\circ$  (Fig. 10c) and also for the initial model with the subhorizontal axis gently dipping in azimuth of  $90^\circ$  (Fig. 10f). In the case of the other two initial orientations of inclined axes (at azimuth of  $0^\circ$  and  $270^\circ$ ) the recovered model is more complex and does not capture well the anisotropy of the

Synthetic model II. At some nodes, even solutions with low-velocity  $b$ -axis occur despite the fact that the target anisotropy is of a high-velocity  $a$ -axis (Figs 10a and d). Such a solution appears when the initial orientation of the symmetry axis is far from the true high-velocity  $a$ -axis of the synthetic model and it is thus closer to the low-velocity ( $b, c$ ) plane of the prescribed hexagonal anisotropy. In the southern block, anisotropy inclined at  $30^\circ$  in azimuth of  $0^\circ$  is recovered well by inversions with the initial inclined or subvertical symmetry axes both in azimuth of  $0^\circ$  (Figs 10a and e).

The sensitivity of resulting models on initial anisotropic parameters calls for being careful when setting the initial parameters for anisotropic tomography. To minimize any potential bias, while modelling the *a priori* unknown anisotropic structure of the Earth's upper mantle, we have looked for a way how to evaluate and present a whole family of anisotropic model parameters retrieved in each node for the set of initial setups. Fig. 11 combines all the output models in such a way that the isotropic components of velocity resulting from all the inversions are averaged in individual nodes,

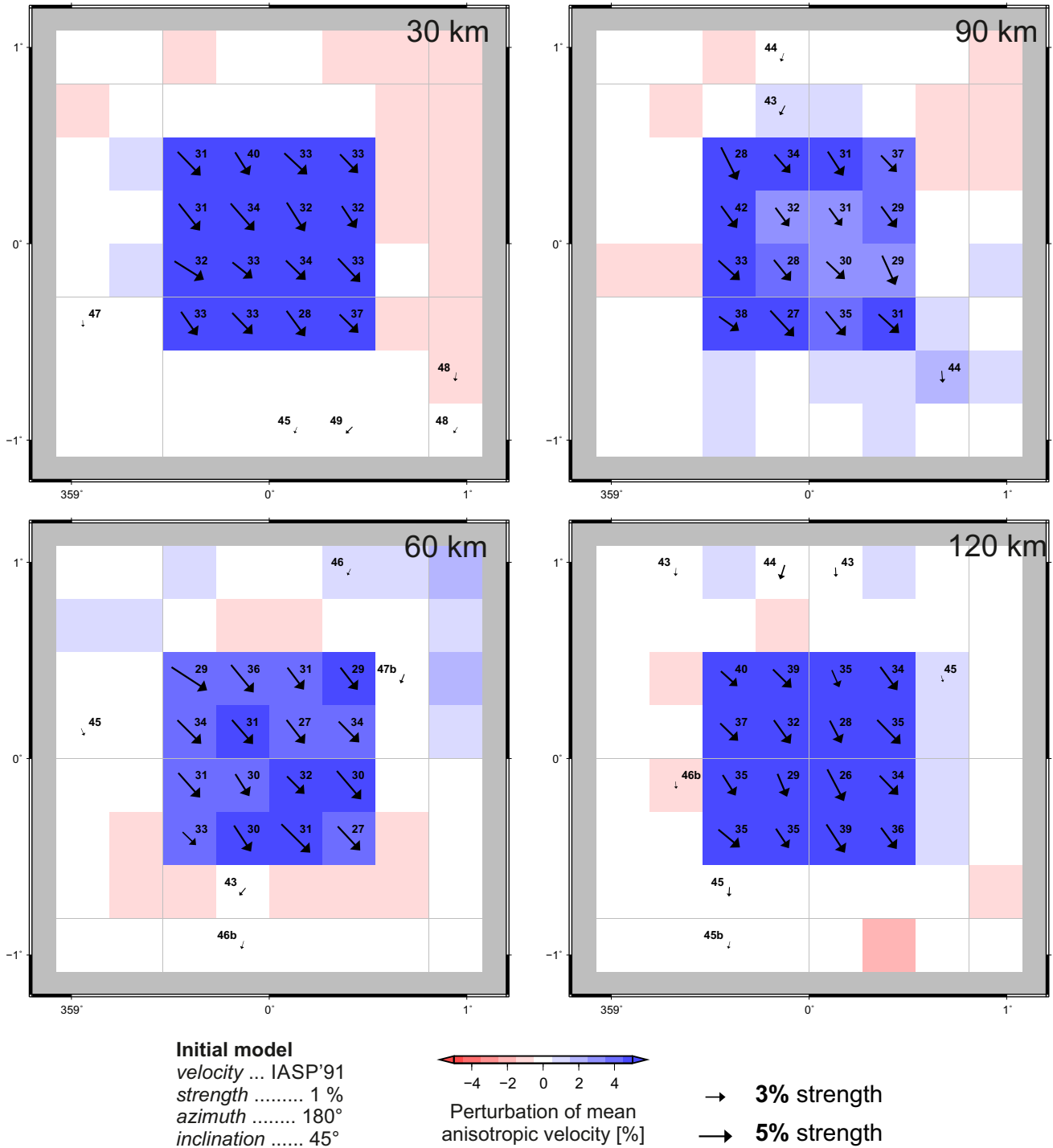


**Figure 8.** The entire model resulting after four iterations of the synthetic inversion with well-tuned damping factors and the initial model close to the target model (Fig. 2). See caption of Fig. 2 for description of visualization of the anisotropic parameters.

while the output strength of anisotropy, the azimuth and inclination of the symmetry axis are displayed individually for each inversion and every grid node. To present the retrieved anisotropy in each node, we plot its strength in stereographic projection on the lower hemisphere, where the two angles represent orientation of symmetry axis.

Fig. 11 displays the combined resulting model at depths of 90 and 150 km (for the whole combined model see Supplementary Fig. S5). We concentrate on distinct features and general trends of the

resulting parameters from inversions with different initial models that are consistent over relatively large regions. The three blocks of the Synthetic model II can be easily distinguished at the depth of 90 km according to all parameters. The red-white-blue background in Fig. 11 expresses the velocity perturbations, whereas the blue and red symbols reflect orientation of the high-velocity and the low-velocity anisotropy axes, respectively. This way of presentation of the results is complex, but allows us to consider all four basic model parameters jointly.

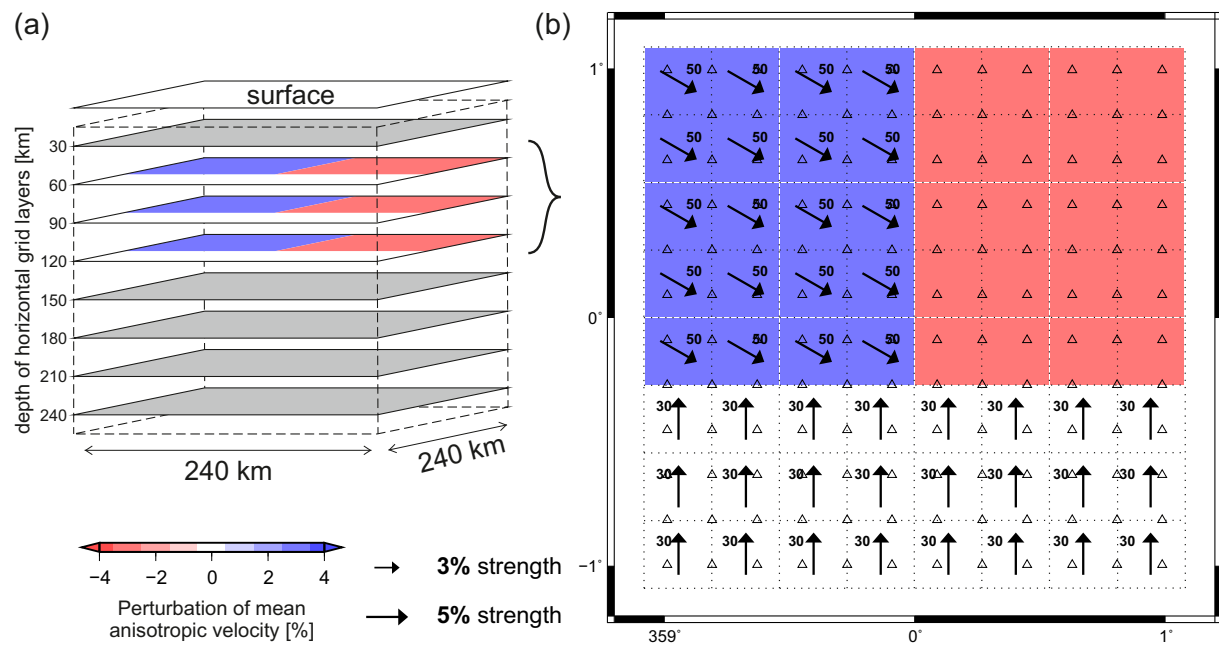


**Figure 9.** Scheme of synthetic model mimicking a realistic anisotropic structure of the mantle lithosphere (a). Three blocks with different mean velocities and anisotropy (b) are put between depths of 45 km and 135 km. Both the northwestern high-velocity and the northeastern low-velocity blocks exhibit 3 per cent amplitude of the isotropic-velocity perturbations. Strength of anisotropy in the northwestern and in the southern blocks is 5 per cent. See caption of Fig. 2 for description of visualization of the anisotropic model and the synthetic station-event distribution.

**Table 1.** Anisotropic parameters of three anisotropic blocks between 45 and 135 km depths of the synthetic model mimicking domains of continental mantle lithosphere (see Fig. 9).

	Vel. pert. from IASP'91 (%)	Strength of anisotropy (%)	Azimuth of symmetry axis (°)	Inclination of symmetry axis (°)
Northwestern b.	3	5	120	50
Northeastern b.	-3	0	NA	NA
Southern b.	0	5	0	30

Shortcut vel. pert. stands for velocity perturbation and b. for block.

The resulting orientations of the high-velocity  $a$ -axis (blue symbols) tend to concentrate in roughly southeastern inclined directions in the northwestern block of the model (within dashed green curve, Fig. 1), which is in agreement with the target anisotropy in the northwestern block. On the other hand, there are also low-velocity  $b$ -axes (red symbols) that incline in approximately opposite, that is in the northwestern directions. These ‘secondary’ solutions with the low-velocity  $b$ -axis have a very similar distribution of directions of relatively high and low velocities for teleseismic  $P$  waves as the target anisotropy with high-velocity  $a$ -axis. Preference of the models with  $b$ -axis is a consequence of a large angular deviation between the corresponding initial axes and the target symmetry axis. Moreover, distribution of the solutions with a low-velocity  $b$ -axis complements at each node the solutions with a high-velocity  $a$ -axis, confirming thus self-consistency and stability of the anisotropic part of the model.

In the south (within dotted green curve), the resulting high-velocity  $a$ -axes concentrate in directions steeply inclined towards the north. On the other hand, the northeastern region does not exhibit distinct signs of anisotropy. The strength of anisotropy is low there (1–2 per cent) and orientations of the output axes are rather diffuse than localized. This indicates that the coupled anisotropic–isotropic inversion does not create any coherent anisotropy in the isotropic northeastern part of the model. In general, structure of the two anisotropic and one isotropic blocks is well recovered (Fig. S5).

and the resulting model captures perfectly sharpness of the block boundaries.

Contrast between the resulting parameters at the depth of 90 km and those at 150 km, representing the topmost isotropic layer below the anisotropic blocks, is evident (Fig. 11). Some leakage of both the isotropic and anisotropic components of velocity below the anisotropic blocks appears due to smearing along the ray paths, which is a typical drawback of teleseismic tomography, but it does not exceed amplitude of 2 per cent of isotropic perturbations and anisotropy strength. Moreover, concentration of symmetry axes towards a particular direction is very limited and it appears only in a few grid cells or at the model edges indicating an artefact. The negative effect of smearing is evident particularly at the 30 km depth, at the upper limit of our model (Fig. S5).

Results of Synthetic test II allows us to conclude that running the anisotropic inversion systematically for different initial orientations of the symmetry axis leads to a robust model of anisotropic velocities.

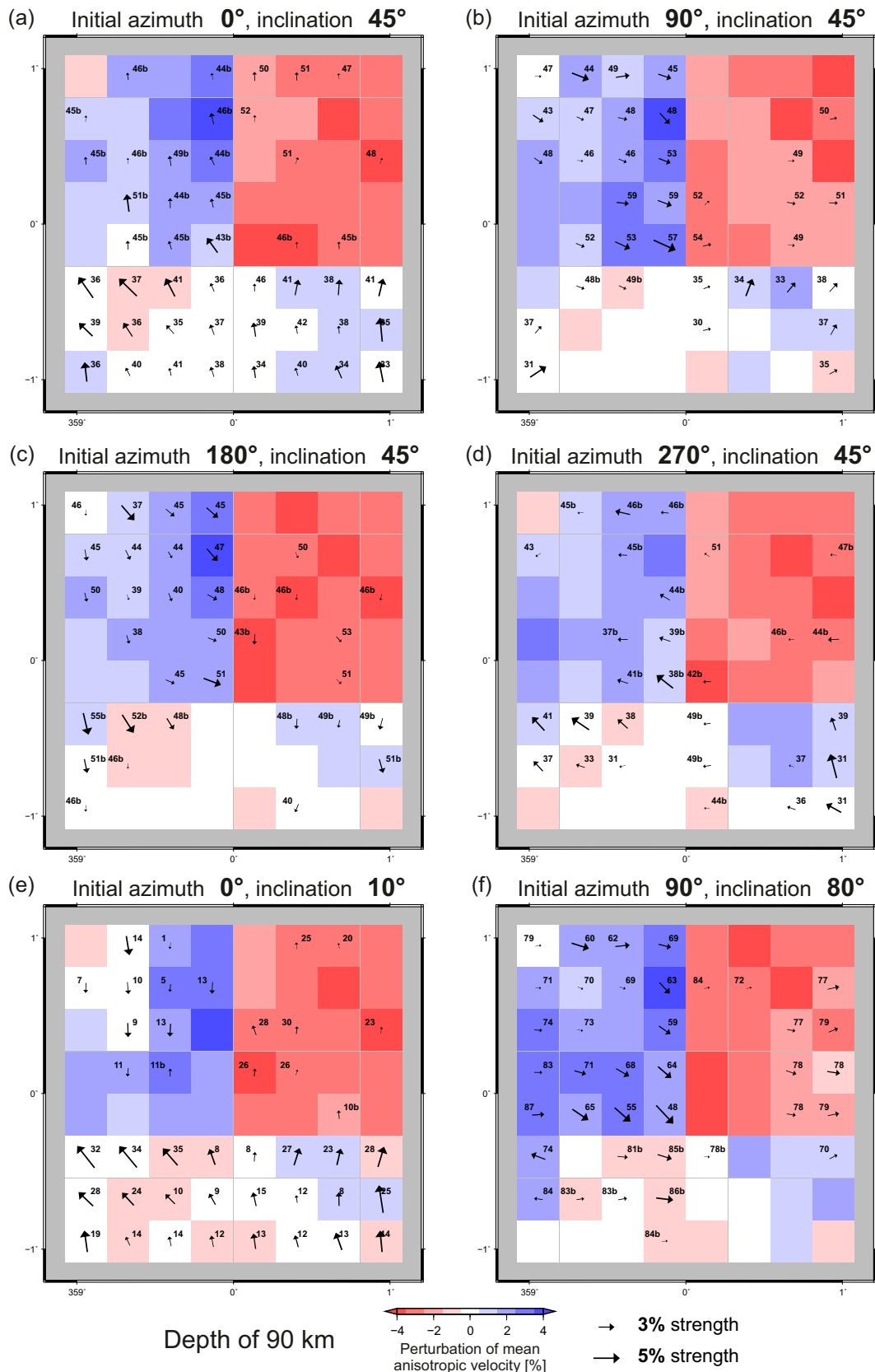


**Figure 10.** Resulting model parameters at 90 km depth after four iterations of synthetic inversions with different initial orientations of the symmetry axis (the models down to 180 km depth are in Fig. S4; synthetic model is in Fig. 9). See caption of Fig. 2 for description of visualization of the anisotropic parameters. Initiating the inversion from an orientation of the symmetry axis that is not much deviated from the searched orientation, the symmetry axis turns in a correct direction during the inversion.

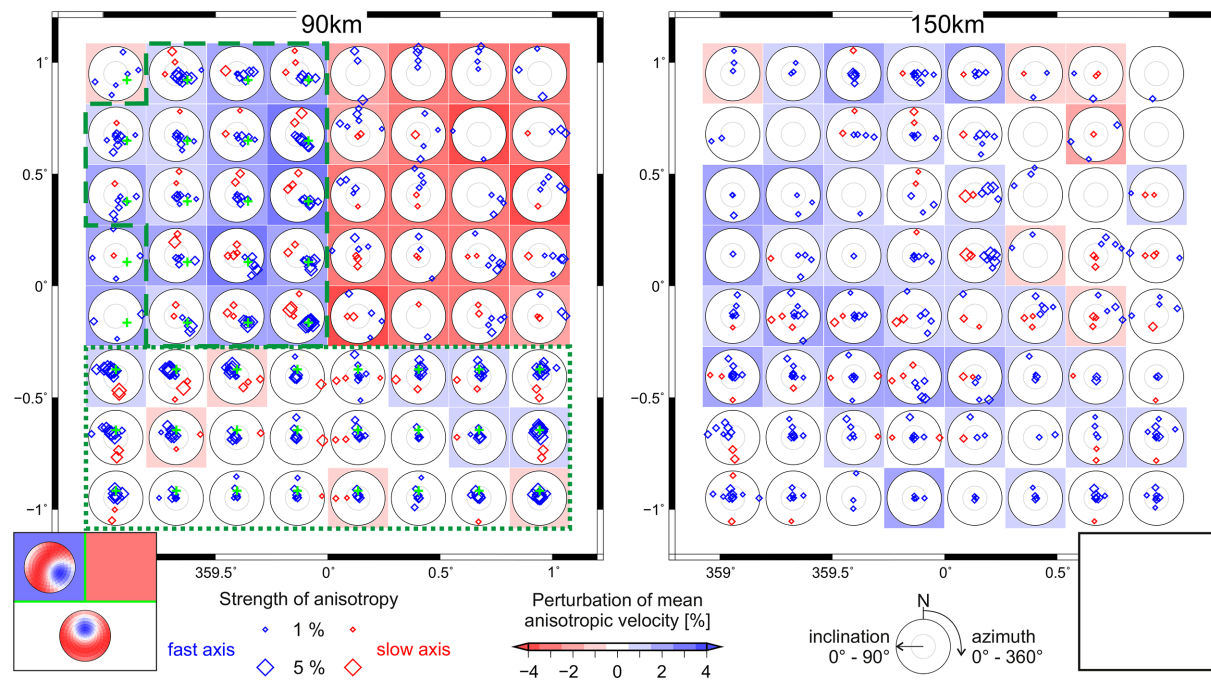


**Figure 11.** Resulting model parameters after four iterations of synthetic inversions with different initial orientations of the symmetry axis imaged together in the combined output model at 90 km and 150 km depths (the whole combined model is in Fig. S5; synthetic model is in Fig. 9). The isotropic components of velocity from the individual inversions are averaged at each node and displayed as background squares in the combined model. Output orientations from individual inversions are imaged as single points at each node represented by blue or red symbols for high-velocity  $a$  or low-velocity  $b$ -axis of hexagonal symmetry, respectively, in lower-hemisphere stereographic projection (white circles). Size of the symbols is scaled by strength of anisotropy and only parameters with strength larger than 1 per cent are plotted, because resolution of symmetry-axis orientation decreases with decreasing strength of anisotropy. The synthetic, that is correct orientations of symmetry axis are marked with green crosses at nodes where non-zero strength is assigned in the synthetic model. The insets also schematically image the input synthetic structure. Dashed, or dotted, green curves delimit regions that exhibit a relatively homogeneous anisotropy associated with the northwestern, or southern, block of the synthetic model, respectively.

### 5.3 Trade-off between isotropic-velocity heterogeneities and anisotropic structure

The previous test shows that the AniTomo code is capable to reveal structures with both anisotropic- and isotropic-velocity components. For further testing of the code, we consider either only the isotropic or only the anisotropic part of the synthetic model imaged in Fig. 9, in order to see how the traveltimes residuals from purely isotropic or purely anisotropic structures are interpreted by the coupled anisotropic-isotropic inversion.

First, we perform the coupled anisotropic-isotropic inversion with the purely isotropic-velocity heterogeneities (Fig. 12 for depths of 90 and 150 km and Fig. S6 for all depth layers). The coupled inversion retrieves the synthetic structure very well. Smearing of the isotropic velocities is very weak and no artificial anisotropy is generated. Anisotropy exceeding 1 per cent strength emerges only sporadically.

In the second step, we invert purely anisotropic structures (Fig. 13 and S7). The coupled inversion retrieves the directions of relatively high and low velocities properly in the blocks where anisotropy is prescribed in the input model, that is in the northwestern and southern blocks. However, some signs of artificial, though very weak anisotropy, can be found at the edge of the originally purely isotropic northeastern block. The strongest artefacts occur in the topmost layer at 30 km depth, where neither anisotropy nor isotropic-velocity variations exist in the synthetic model (Fig. S7). The anisotropic patterns in the northwest and south of the 30 km layer meet the orientations of the deeper layers and they result from upward smearing of the strongly anisotropic structures at 60–120 km. On the other hand,

the low-velocity perturbations in the central and northeastern parts of the 30 km layer, together with the highly spread high-velocity axes of anisotropy in the northeast, are isolated. This structure is a strong artefact, but it is limited to the topmost, less resolved, layer (Fig. 14). The low-velocity heterogeneity possibly arises from upward smearing of accordingly oriented low-velocity directions in the northwestern and southern blocks. The spread high-velocity axes in the northeast emerge possibly to compensate the artificial low-velocity heterogeneity in the central part. The deeper parts of the output model, evaluated for the purely anisotropic input, are contaminated by false isotropic-velocity perturbations reaching mostly 1 per cent and locally 2 per cent amplitude (Fig. S7). This test has shown that isotropic-velocity artefacts can be generated from anisotropic input velocities by the coupled anisotropic-isotropic inversion, particularly in the topmost part of the model, where there is not sufficient cross-firing of the rays (see also Fig. 14).

Another test is a standard isotropic-velocity inversion with the same synthetic model consisting of the anisotropic structure of the blocks at depths of 60, 90 and 120 km. Thus, the traveltimes residuals caused by anisotropy are forced to be interpreted only as isotropic-velocity perturbations (Fig. S8). Distribution of the low and high isotropic-velocity perturbations is similar to that imaged by the coupled anisotropic-isotropic inversion (Fig. 13 and S7), but the amplitudes are stronger. Reduction of data variance, that is (initial variance—final variance)/initial variance, is 64 per cent for the isotropic-velocity inversion. Evaluation of variance reduction for the coupled anisotropic-isotropic inversion (Fig. 13 and S7) is not as straightforward as in the isotropic case, because we can calculate

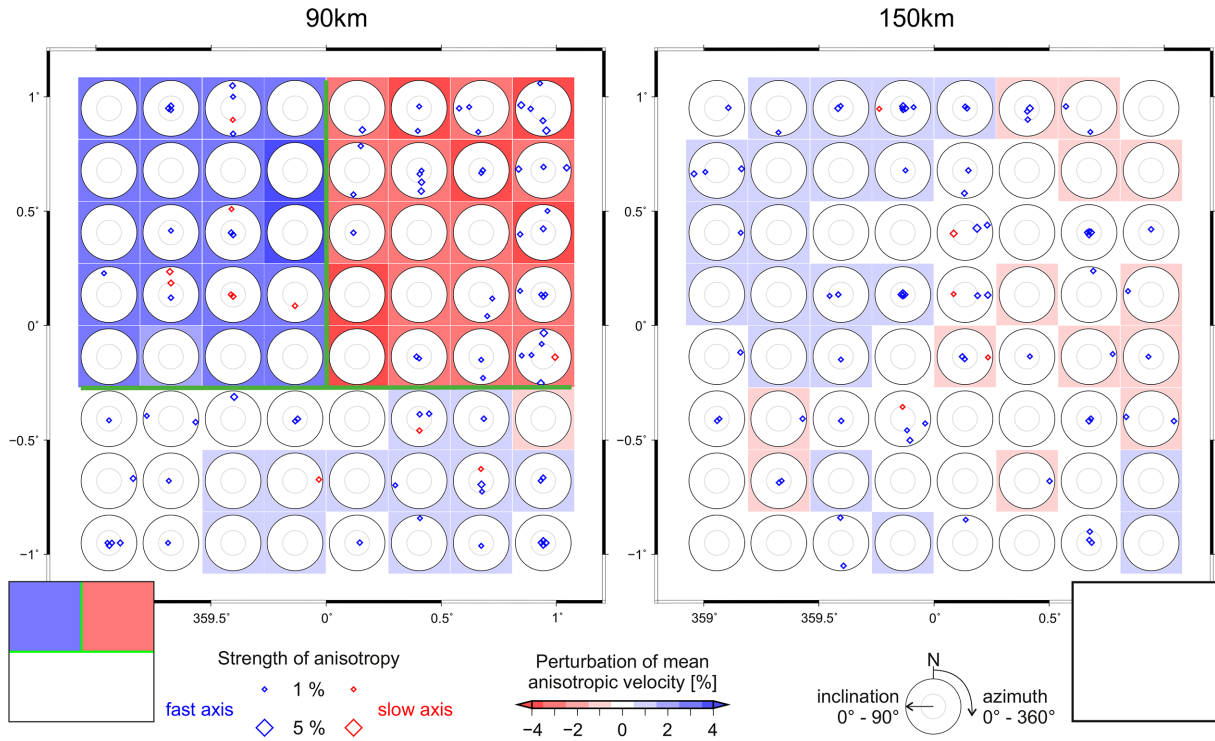


**Figure 12.** Depth sections at 90 and 150 km of the model of anisotropic velocities resulting from coupled anisotropic-isotropic inversion of synthetic traveltime residuals calculated for  $P$  waves propagating through the isotropic part of the structure imaged in Fig. 9 (see also the insets at the bottom of each depth section). See Fig. 11 for more details.

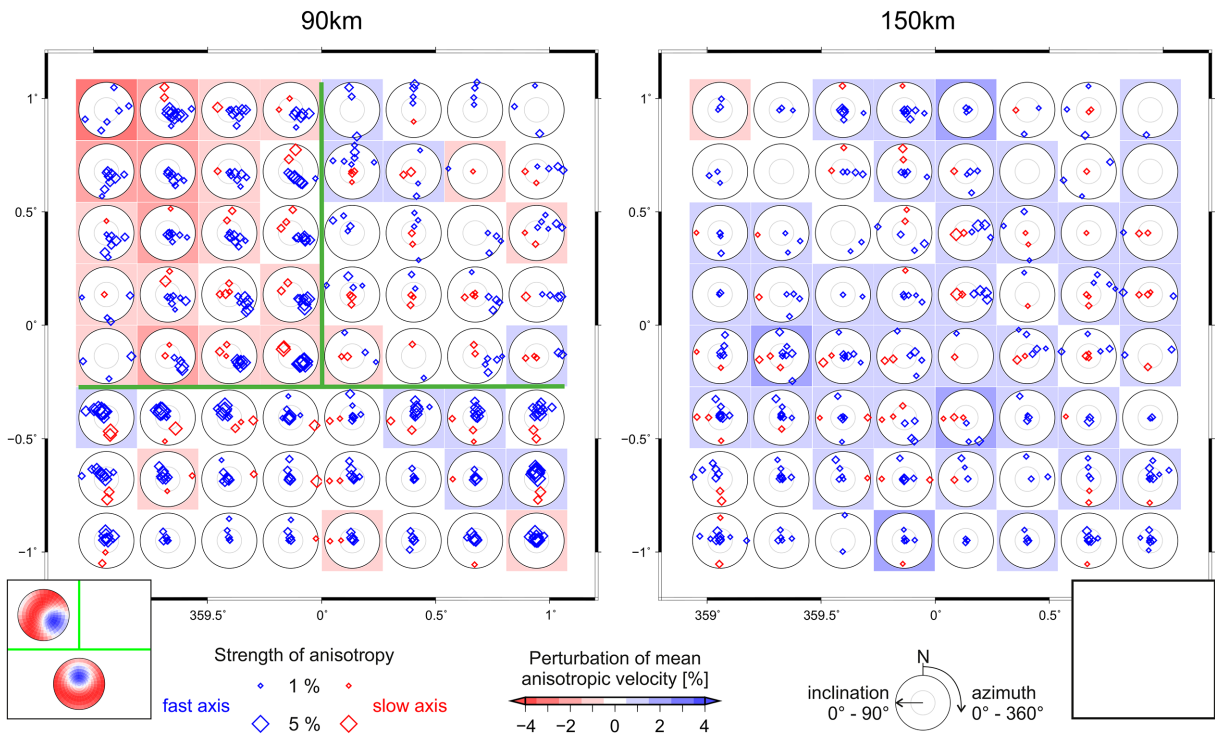


**Figure 13.** Depth sections at 90 and 150 km of the model of anisotropic velocities resulting from coupled anisotropic-isotropic inversion of synthetic traveltime residuals calculated for  $P$  waves propagating through the anisotropic part of the structure imaged in Fig. 9 (see also the insets at the bottom of each depth section). See Fig. 11 for more details.

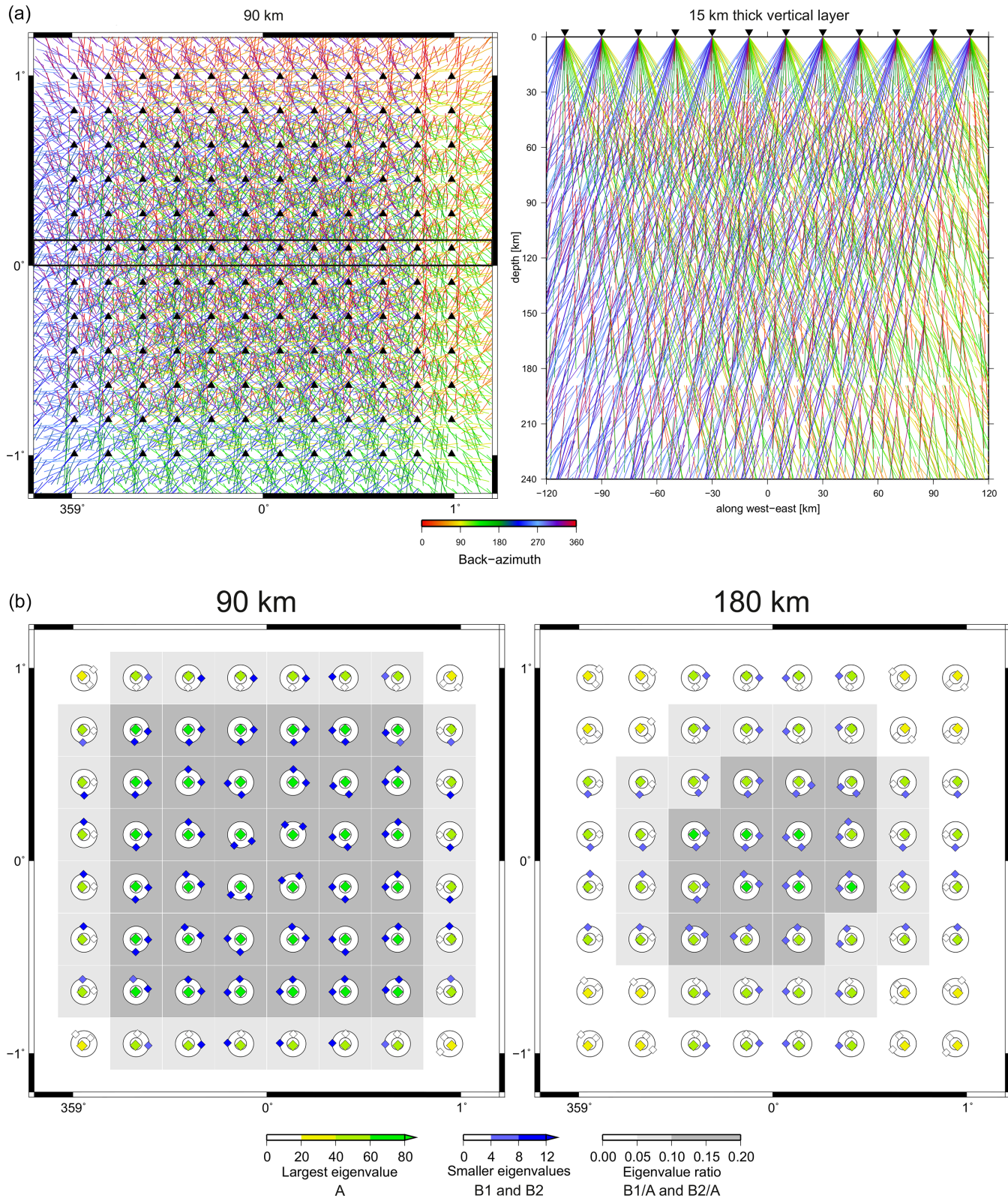


**Figure 14.** (a) Ray paths of the synthetic set of equally distributed teleseismic events (Fig. 2b) within depth layer of 90 km and within a vertical layer of 15 km thickness oriented west–east (marked with horizontal black lines in the map on the left). The ray paths are coloured according to wave backazimuth. Triangles represent the equally distributed receivers. (b) Ray density tensors (RDT) evaluated for the parametrization nodes of the 90 and 180 km depths for our set of equally distributed synthetic rays. Orientation of three RDT eigenvectors of each node is imaged with points displayed in the lower-hemisphere stereographic projection. Size of the largest RDT eigenvalue of a node is displayed with a different colour scale (marked as A) than size of the two smaller eigenvalues (marked as B1 and B2). Ratios between the smaller eigenvalues and the largest eigenvalue at a node, that is  $B1 A^{-1}$  and  $B2 A^{-1}$ , are imaged with a background colour. Both the ratios must be larger than the lower limit of a colour band to mark the node with that colour. Such a visualization of RDT eigenvalues and eigenvectors enables to distinguish the nodes according to quality of their ray coverage.

this measure just for each inversion of the set of anisotropic inversions. Nevertheless, even for the individual anisotropic inversions, the data variance reduction attains values from 71 to 86 per cent and thus increases compared to the isotropic case.

Alternatively, we can fix the isotropic-velocity perturbations and invert only for the strength of anisotropy and orientation of the symmetry axis (Fig. S9). The variance reduction of the individual inversions varies from 66 to 85 per cent. The anisotropic artefacts similar to those in Fig. S7 above and beneath the anisotropic blocks remain, but the structure of the three blocks is imaged correctly and very clearly.

Results of the isotropic-velocity inversion, when the input velocity model is purely anisotropic, depend on distributions and orientations of anisotropy. Some of them are more prone to be misinterpreted as isotropic velocities than others. For example, we perform such a test also with a synthetic model where in the northwestern block the symmetry axis still dips to the southeast, but the type of the axis is changed from high- to low-velocity. It means that the directions of relatively high and low velocities are reversed. After the purely isotropic inversion, data variance for that anisotropic input is reduced only by 40 per cent. In the previous case, in which the high-velocity axis dips to the southeast in the northwestern block, the variance reduction was 64 per cent. This reflects the fact that the convergently oriented high-velocity directions in the two anisotropic blocks favour creation of a high-velocity region beneath them (Fig. S7). Thus, a larger part of the traveltimes residuals due to the anisotropic input can be absorbed by the isotropic-velocity perturbations in the output model.

To summarize the last synthetic tests, the coupled anisotropic-isotropic inversion does not tend to create anisotropic artefacts when the real structure is purely isotropic. In the case of anisotropic structure, the situation is more complex. A part of the anisotropic contribution to velocity might be misinterpreted either as an isotropic component or as localized, usually weaker, anisotropy smeared into the isotropic part. Nevertheless, regions of distinct anisotropy and isotropic-velocity heterogeneities are identified correctly. Such findings represent a great benefit of the coupled anisotropic-isotropic inversion compared to a purely isotropic inversion, which misinterprets the anisotropic signal completely.

#### 5.4 Ray density tensor—A tool to investigate distribution of the rays

Quality of directional coverage of the volume studied by rays is crucial to retrieve anisotropic velocities. Fig. 14(a) shows segments of ray paths lying in the horizontal layer at 90 km depth and within a vertical layer of 15 km thickness. The synthetic set of rays used in this paper is realistic for teleseismic  $P$  waves, but idealistic regarding their uniform distribution. With such an evenly distributed set of rays, we avoid biasing the presented tests, focusing on other aspects of the method by any directional asymmetry (see Munzarová *et al.* 2018, revision submitted, for anisotropic tomography with a real ray distribution). Teleseismic  $P$  waves propagate within the upper mantle at angles between  $\sim 20^\circ$  and  $\sim 50^\circ$  and thus the waves are sensitive particularly to anisotropy with inclined symmetry axes.

AniTomo enables evaluation of so-called ray density tensors (RDT; Appendix B) which is a tool to represent directional coverage of a volume studied by a set of rays. Fig. 14(b) shows orientation of eigenvectors and size of eigenvalues of RDT at the nodes of depth of 90 and 180 km of our parametrization grid. The images indicate not only an overall amount of the rays within the parametrization

cells (size of the eigenvalues), but they also express directional evenness of the ray distribution (orientation of the eigenvectors and ratio between the eigenvalues). One of the eigenvalues ( $A$ ) is always much larger than the other two RDT eigenvalues ( $B1$  and  $B2$ ), which is caused by the limited incidence angles of the teleseismic  $P$  waves. The more vertical orientation of the eigenvector belonging to the largest eigenvalue (green or yellow dots), the more even azimuthal coverage of the parametrization cell by the teleseismic rays we have. In our case of quasi-equally distributed rays, orientation of the eigenvectors with the largest eigenvalues is vertical for the central part of the individual depth layers and inclines towards the model edges (Fig. 14b). A simplified way how to express evenness of the directional coverage is to investigate ratios of the smaller eigenvalues to the largest eigenvalue, that is  $B1\ A^{-1}$  and  $B2\ A^{-1}$ . We can see that ratios  $B1\ A^{-1}$  and  $B2\ A^{-1}$  in a range from 0.1 to 0.2 (grey background colours in Fig. 14b) ensure a very good recovery of the anisotropic parameters according to the results of the synthetic tests (Sections 4 and 5).

## 6 DISCUSSION

We present new code AniTomo for anisotropic teleseismic tomography of the upper mantle, and focus in details on its functionality and potential limitations. Careful tuning of the inversion setup is important in order to get robust and reliable models as we have demonstrated in a methodological series of synthetic tests (Section 4). Damping factors directly affect stability of the inversion, rate of convergence of the model parameters with number of iterations and their scatter. Testing a range of various damping factors before selecting the final values should represent a routine step for any kind of regularized inversion. In the case of anisotropic tomography, different physical meaning of model parameters, that is perturbation of the isotropic component of anisotropic velocity, strength of anisotropy, azimuth and inclination of the symmetry axis, imposes specific demands on the selection of damping. Although regularization of all model parameters decides about success and reliability of the inversion, only little can be found in publications on tomography of azimuthal or radial velocities of the body waves. Huang & Zhao (2013) and Tian & Zhao (2013) show at least a trade-off curve for various damping values of velocity perturbations, but the way of treating the other model parameters remains unspecified.

The general strategy how a complex anisotropic heterogeneous structure can be retrieved with AniTomo is demonstrated in Section 5 on a synthetic block-like structure mimicking domains of the continental mantle lithosphere. The non-linearity of the relation between anisotropic velocity and orientation of the symmetry axis (eq. 8) calls for repeating the inversion several times, starting always from a different initial orientation of the symmetry axis, to systematically cover the whole range of initial conditions. The solution of a particular inversion depends in each node on a deviation between the initial and the searched orientations of the symmetry axis. If the deviation is smaller than about  $60^\circ$ , a distinct anisotropy with a systematic convergence towards the correct orientation easily develops within a few iterations. On the other hand, the parameters converge more slowly when the deviation is large or the searched velocities are isotropic. If the output anisotropic parameters, returned from inversions with different initial axis orientations, tend to create similar pattern, it is an indication of reliability of that anisotropic feature. For a real application of AniTomo, some of the initial models could also be based on *a priori* information on anisotropy in the region if available from other geophysical methods and data sets.

Anisotropy and isotropic heterogeneities affect  $P$ -wave propagation and it is not simple to discriminate between these two sources of traveltime deviations. But in general, large-scale anisotropy can hardly be fully mimicked by a large-scale isotropic structure, or vice versa. We perform a series of synthetic tests with the coupled anisotropic–isotropic inversion to assess the potential trade-off between effects of isotropic-velocity heterogeneity and seismic anisotropy. Our synthetic tests document that the coupled anisotropic–isotropic inversion with AniTomo successfully distinguishes both effects, though indistinctive isotropic- or anisotropic-velocity artefacts might occur, particularly at the edges of the structures. Some distortions of the velocities come from well-known subvertical smearing which is a general drawback of teleseismic tomography. On the other hand, running only purely isotropic inversion, when the target structure is anisotropic leads to misinterpretations in the resulting models as we show in our synthetic tests (Section 5.3). Advantage of the developed coupled anisotropic–isotropic inversion is that it does not create anisotropic artefacts when the real structure is purely isotropic.

Although our synthetic data set is realistic as to number of rays and range of incidence angles of teleseismic  $P$  waves, the quasi-equality of event distribution is idealistic. To achieve a good recovery of the isotropic component of velocity and the anisotropy a good station-event distribution is crucial. For the purpose of analysing directional coverage of a volume by rays in 3-D, we have implemented calculation of so-called ray density tensors (RDT; Appendix B). RDT evaluated for the equally distributed rays with realistic teleseismic incidence angles (Section 5.4) can serve as a benchmark for future comparison with ray geometry of real seismic experiments (Munzarová *et al.* 2018, revision submitted). On the basis of such an analysis, the inversion of real data can be adjusted to actual ray distribution, for example by turning off the inversion for strength of anisotropy and orientation of the symmetry axis at weakly covered parametrization cells. Similarly to our ray density tensors, Huang *et al.* (2015) define normalized length of short axis (NLS) of an ellipse approximating distribution of ray backazimuth and incidence angles in the case of local-earthquake traveltimes inversion for azimuthal and radial anisotropy, respectively. Based on synthetic tests, these authors conclude that inversion at the nodes with NLS parameter as low as 0.3 still yields only a small trade-off between heterogeneities and anisotropy. In this context, our ratios of the two smaller eigenvalues to the largest eigenvalue of the RDT for the synthetic set of purely teleseismic rays (Section 5.4) in a range from 0.1 to 0.2 do seem reasonable. Such ratios of a smaller to the largest eigenvalue describe the strong directional variation of the ray distribution within any subvertical plane as the largest eigenvalue is always subvertical for our set of teleseismic rays. On the contrary, a ratio between the two smaller eigenvalues can be associated with the azimuthal ray coverage, which is, of course, much better in our case as the two smaller eigenvalues are comparable.

Teleseismic  $P$  waves propagate in the upper mantle at angles between 20° and 50° and thus they can detect very well anisotropy with inclined symmetry axis (e.g. Babuška *et al.* 1984; Grésillaud & Cara 1996). Recovery of a horizontal axis is more difficult with AniTomo as it was confirmed by a synthetic test (not presented in this paper), during which a layer of anisotropy with horizontal symmetry axis was restored only partly by the inversion. For the same reason of limited incidence angles of teleseismic  $P$  waves, AniTomo can not always distinguish between hexagonal symmetry with inclined high-velocity  $a$ -axis perpendicular to low-velocity plane ( $b,c$ ) and low-velocity  $b$ -axis perpendicular to high-velocity

plane ( $a,c$ ) (Fig. S1a). However, both types of hexagonal symmetry are considered in the code because they are physically reasonable and distinguishing between them can be supported by combination of various methods (e.g. Plomerová & Babuška 2010; Plomerová *et al.* 2011). Moreover, allowing for both types of the symmetry (either with  $a$ - or  $b$ -axis) increases chance for the model parameters to converge towards one of the solutions, because it is easier to change strength of anisotropy than to rotate the symmetry axis during inversion, and hence to capture the relatively high- and low-velocity directions of anisotropy (Section 5.2).

## 7 CONCLUSIONS

Widely spread detection of seismic anisotropy of the continental mantle lithosphere called for formulating theory and developing novel tomographic code AniTomo that retrieves 3-D heterogeneous weakly anisotropic structure of the upper mantle. The code iteratively solves the coupled problem of the 3-D anisotropic velocity field by inversion of traveltimes residuals of teleseismic  $P$  waves for parameters describing weak anisotropy with hexagonal symmetry. The model parameters are perturbations of isotropic component of anisotropic velocity, strength of anisotropy and azimuth and inclination of the symmetry axis oriented generally in 3-D. Current version of AniTomo is applicable only to  $P$  waves and not to  $S$  waves, for which anisotropic propagation is much more complex.

The main conclusions from the series of realistic synthetic tests that document functionality of code AniTomo as well as effects of inversion setup on the results are:

- (1) The coupled anisotropic–isotropic inversion with AniTomo can successfully distinguish isotropic- and anisotropic components of  $P$ -wave velocity even for complex block-like structures of the upper mantle.
- (2) The coupled anisotropic–isotropic inversion does not create anisotropic artefacts when the real structure is purely isotropic.
- (3) Isotropic- or anisotropic-velocity artefacts with amplitude mostly of ~1 per cent might occur in the resulting model, particularly towards the edges of the structures. Strength of anisotropy was 5 per cent in those tests.
- (4) Damping factors of all parameters, well-tuned according to synthetic tests, help to achieve a steady convergence towards the correct solution.
- (5) Series of inversions with systematically changing initial orientation of anisotropy reduces effects due to a subjective choice of the initial setup.
- (6) Similarly to standard isotropic tomography, only signatures consistent over relatively large regions and with similar trends for various initial models should be considered in interpreting of the output parameters.

In the next step, we apply the AniTomo code to data from passive seismic experiment LAPNET to unravel structure of the upper mantle beneath northern Fennoscandia (Munzarová *et al.* 2018, revision submitted) and subsequently to data from other tectonic provinces, for example in the Alpine area, Bohemian Massif or in other parts of Fennoscandia. Tomographic results from AniTomo will contribute to exploration of velocities of anisotropic and heterogeneous upper mantle.

## ACKNOWLEDGEMENTS

The research was supported by grant no. M100121201 of the Czech Academy of Sciences, by grant no. 111-10/253101 of the Grant Agency of Charles University and by project CzechGeo/EPOS-Sci, no. CZ.02.1.01/0.0/0.0/16\_013/0001800, financed from the Operational Programme Research, Development and Education within ERDF. We would like to thank to Dr Lapo Boschi, Editor of GJI, and to two anonymous reviewers for their thorough review that helped to improve the manuscript. Figures were plotted with the use of the Generic Mapping Tools (Wessel & Smith 1998).

## REFERENCES

- Aki, K. & Kaminuma, K., 1963. Phase velocity of Love waves in Japan, Part 1. Love waves from Aleutian shock of March 9, 1957, *Bull. Earthq. Res. Inst.*, **41**, 243–259.
- Anderson, D.L., 1961. Elastic wave propagation in layered anisotropic media, *J. geophys. Res.*, **82**, 277–296.
- Anderson, D.L. & Dziewonski, A.M., 1982. Upper mantle anisotropy: evidence from free oscillations, *Geophys. J. R. astr. Soc.*, **69**, 383–404.
- Arlitt, R., Kissling, E. & Ansorge, J., 1999. Three-dimensional crustal structure beneath the TOR array and effects on teleseismic wavefronts, *Tectonophysics*, **314**, 309–319.
- Auer, L., Boschi, L., Becker, T.W., Nissen-Meyer, T. & Giardini, D., 2014. Savani: a variable resolution whole-mantle model of anisotropic shear velocity variations based on multiple data sets, *J. geophys. Res.*, **119**, 3006–3034.
- Babuška, V. & Cara, M., 1991. *Seismic Anisotropy in the Earth*, Kluwer Academic Publishers.
- Babuška, V. & Plomerová, J., 1992. The lithosphere in central Europe—seismological and petrological aspects, *Tectonophysics*, **207**, 141–163.
- Babuška, V. & Plomerová, J., 1993. Lithosphere thickness and velocity anisotropy—seismological and geothermal aspects, *Tectonophysics*, **225**, 79–89.
- Babuška, V. & Plomerová, J., 2006. European mantle lithosphere assembled from rigid microplates with inherited seismic anisotropy, *Phys. Earth planet. Inter.*, **158**, 264–280.
- Babuška, V., Plomerová, J. & Šílený, J., 1984. Spatial variations of Presiduals and deep-structure of the European lithosphere, *Geophys. J. R. astr. Soc.*, **79**, 363–383.
- Babuška, V., Plomerová, J. & Šílený, J., 1993. Models of seismic anisotropy in the deep continental lithosphere, *Phys. Earth planet. Inter.*, **78**, 167–191.
- Backus, G.E., 1965. Possible forms of seismic anisotropy of the uppermost mantle under oceans, *J. geophys. Res.*, **70**, 3429–3439.
- Becker, T.W., Lebedev, S. & Long, M.D., 2012. On the relationship between azimuthal anisotropy from shear wave splitting and surface wave tomography, *J. geophys. Res.*, **117**, B01306, doi:10.1029/2011JB008705.
- Ben Ismail, W. & Mainprice, D., 1998. An olivine fabric database: an overview of upper mantle fabrics and mantle anisotropy, *Tectonophysics*, **296**, 145–157.
- Bezada, M.J., Faccenda, M. & Toomey, D.R., 2016. Representing anisotropic subduction zones with isotropic velocity models: A characterization of the problem and some steps on a possible path forward, *Geochem. Geophys. Geosyst.*, **17**, 3164–3189.
- Bruneton, M., Pedersen, H.A., Farra, V., Arndt, N.T. & Vacher, P. & SVEKALAPKO Seismic Tomography Working Group, 2004. Complex lithospheric structure under the central Baltic Shield from surface wave tomography, *J. geophys. Res.*, **109**, B10303.
- Chang, S.J., Ferreira, A.M.G., Ritsema, J., van Heist, H.J. & Woodhouse, J.H., 2015. Joint inversion for global isotropic and radially anisotropic mantle structure including crustal thickness perturbations, *J. geophys. Res.*, **120**, 4278–4300.
- Chyba, J., Plomerová, J., Vecsey, L. & Munzarová, H., 2017. Tomography study of the upper mantle around the TESZ based on PASSEQ experiment data, *Phys. Earth planet. Inter.*, **266**, 29–38.
- Debayle, E., Dubuffet, F. & Durand, S., 2016. An automatically updated S-wave model of the upper mantle and the depth extent of azimuthal anisotropy, *Geophys. Res. Lett.*, **43**(2), 674–682.
- Eberhart-Phillips, D. & Henderson, C.M., 2004. Including anisotropy in 3-D velocity inversion and application to Marlborough, New Zealand, *Geophys. J. Int.*, **156**(2), 237–254.
- Eken, T., Shomali, H., Roberts, R. & Bödvarsson, R., 2007. Upper mantle structure of the Baltic Shield below the Swedish National Seismological Network (SNSN) resolved by teleseismic tomography, *Geophys. J. Int.*, **169**, 617–630.
- Fichtner, A., Kennett, B.L.N., Igel, H. & Bunge, H.P., 2010. Full waveform tomography for radially anisotropic structure: New insights into present and past states of the Australasian upper mantle, *Earth planet. Sci. Lett.*, **290**, 270–280.
- Fichtner, A., Saygin, E., Taymaz, T., Cupillard, P., Capdeville, Y. & Trampert, J., 2013. The deep structure of the North Anatolian fault zone, *Earth planet. Sci. Lett.*, **373**, 109–117.
- Fouch, M.J. & Rondenay, S., 2006. Seismic anisotropy beneath stable continental interiors, *Phys. Earth planet. Inter.*, **158**, 292–320.
- French, S.W. & Romanowicz, B.A., 2014. Whole-mantle radially anisotropic shear velocity structure from spectral-element waveform tomography, *Geophys. J. Int.*, **199**(3), 1303–1327.
- Gou, T., Zhao, D., Huang, Z. & Wang, L., 2018. Anisotropic 3-D ray tracing and its application to Japan subduction zone, *J. geophys. Res.*, **123**, doi:10.1029/2017JB015321.
- Grésillaud, A. & Cara, M., 1996. Anisotropy and P-wave tomography: a new approach for inverting teleseismic data from a dense array of stations, *Geophys. J. Int.*, **126**, 77–91.
- Hirahara, K. & Ishikawa, Y., 1984. Travel time inversion for three-dimensional P-wave velocity anisotropy, *J. Phys. Earth*, **32**, 197–218.
- Ho, T., Priestley, K. & Debayle, E., 2016. A global horizontal shear velocity model of the upper mantle from multimode Love wave measurements, *Geophys. J. Int.*, **207**(1), 542–561.
- Huang, Z. & Zhao, D., 2013. Mapping P-wave azimuthal anisotropy in the crust and upper mantle beneath the United States, *Phys. Earth planet. Inter.*, **225**, 28–40.
- Huang, Z., Zhao, D. & Liu, X., 2015. On the trade-off between seismic anisotropy and heterogeneity: numerical simulations and application to Northeast Japan, *J. geophys. Res.*, **120**, 3255–3277.
- Hua, Y., Zhao, D. & Xu, Y., 2017. P wave anisotropic tomography of the Alps, *J. geophys. Res.*, **122**, 4509–4528.
- Ishise, M., Miyake, H. & Koketsu, K., 2015. Dual subduction tectonics and plate dynamics of central Japan Shown by three-dimensional P-wave anisotropic structure, *Phys. Earth planet. Inter.*, **244**, 49–68.
- Ishise, M. & Oda, H., 2005. Three-dimensional structure of P-wave anisotropy beneath the Tohoku district, northeast Japan, *J. geophys. Res.*, **110**, B07304, doi:10.1029/2004JB003599.
- Ishise, M. & Oda, H., 2008. Subduction of the Philippine Sea slab in view of P-wave anisotropy, *Phys. Earth planet. Inter.*, **166**, 83–96.
- Karousová, H., 2013. Teleseismic Tomography of the Upper Mantle beneath the Bohemian Massif, *PhD thesis*, Department of Geophysics, Faculty of Mathematics and Physics, Charles University, Prague, Czech Republic.
- Karousová, H., Plomerová, J. & Babuška, V., 2013. Upper-mantle structure beneath the southern Bohemian Massif and its surroundings imaged by high-resolution tomography, *Geophys. J. Int.*, **194**, 1203–1215.
- Karousová, H., Plomerová, J. & Vecsey, L., 2012. Seismic tomography of the upper mantle beneath the north-eastern Bohemian Massif (central Europe), *Tectonophysics*, **564–565**, 1–11.
- Kennett, B. & Engdahl, R., 1991. Travel times for global earthquake location and phase identification, *Geophys. J. Int.*, **105**, 429–465.
- Kennett, B.L.N., Engdahl, E.R. & Buland, R., 1995. Constraints on seismic velocities in the earth from travel times, *Geophys. J. Int.*, **122**, 108–124.
- Kissling, E., 1988. Geotomography with local earthquake data, *Rev. Geophys.*, **26**, 659–698.
- Kissling, E. & Spakman, W., 1996. Interpretation of tomographic images of uppermost mantle structure: examples from the western and central Alps, *J. Geod.*, **21**, 97–111.

- Koulakov, I., Kukarina, E., Fathi, I., Khrepy, S. & Al-Arifi, N., 2015. Anisotropic tomography of Hokkaido reveals delamination-induced flow above a subducting slab, *J. geophys. Res.*, **120**, 3219–3239.
- Kustowski, B., Ekström, G. & Dziewoński, A.M., 2008. Anisotropic shear-wave velocity structure of the Earth's mantle: a global model, *J. geophys. Res.*, **113**, B06306, doi:10.1029/2007JB005169.
- Lippitsch, R., Kissling, E. & Ansorge, J., 2003. Upper mantle structure beneath the Alpine orogen from high-resolution teleseismic tomography, *J. geophys. Res.*, **108**, B82376, doi:10.1029/2002JB002016.
- Liu, X. & Zhao, D., 2016. Seismic velocity azimuthal anisotropy of the Japan subduction zone: constraints from P and S wave traveltimes, *J. geophys. Res.*, **121**, 5086–5115.
- Liu, X. & Zhao, D., 2017a. P-wave anisotropy, mantle wedge flow and olivine fabrics beneath Japan, *Geophys. J. Int.*, **210**, 1410–1431.
- Liu, X. & Zhao, D., 2017b. Depth-varying azimuthal anisotropy in the Tohoku subduction channel, *Earth planet. Sci. Lett.*, **473**, 33–43.
- Long, M.D. & Becker, T.W., 2010. Mantle dynamics and seismic anisotropy, *Earth planet. Sci. Lett.*, **297**, 341–354.
- Long, M.D. & Silver, P.G., 2009. Shear-wave splitting and mantle anisotropy: measurements, interpretations, and new directions, *Surv. Geophys.*, **30**, 407–461.
- Mainprice, D., 2007. Seismic anisotropy of the deep Earth from a mineral and rock physics perspective, in *Treatise on Geophysics*, pp. 437–491, ed. Schubert, G., Elsevier, Oxford, UK.
- Maupin, V. & Park, J., 2007. Theory and observations—wave propagation in anisotropic media, in *Treatise on Geophysics*, Vol. 1: Seismology and the Structure of the Earth, pp. 289–321, eds Romanowicz, B. & Dziewoński, A., Elsevier, doi:10.1016/B978-044452748-6.00007-9.
- Menke, W., 1984. *Geophysical Data Analysis: Discrete Inverse Theory*, 1st edn, Academic Press, Inc.
- Menke, W., 2015. Equivalent heterogeneity analysis as a tool for understanding the resolving power of anisotropic travel-time tomography, *Bull. seism. Soc. Am.*, **105**, 719–733.
- Montagner, J.P., 1994. Can seismology tell us anything about convection in the mantle? *Rev. Geophys.*, **32**, 115–137.
- Montagner, J.P., 1998. Where can seismic anisotropy be detected in the Earth's mantle? In boundary layers, *Pure appl. Geophys.*, **151**, 223–256.
- Montagner, J.P. & Kennett, B.L.N., 1996. How to reconcile body-wave and normal-mode reference Earth models? *Geophys. J. Int.*, **125**, 229–248.
- Montagner, J.P. & Nataf, H.C., 1986. A simple method for inverting the azimuthal anisotropy of surface waves, *J. geophys. Res.*, **91**, 511–520.
- Munzarová, H., Plomerová, J., Kissling, E., Vecsey, L. & Babuška, V., 2018. Novel anisotropic teleseismic body-wave tomography code AniTomo to illuminate heterogeneous anisotropic upper mantle: Part II - Application to data of passive seismic experiment LAPNET in northern Fennoscandia, *Geophys. J. Int.*, revision submitted.
- Nita, B., Maurya, S. & Montagner, J.P., 2016. Anisotropic tomography of the European lithospheric structure from surface wave studies, *Geochem. Geophys. Geosyst.*, **17**, 2015–2033.
- Panning, M. & Romanowicz, B., 2006. A three-dimensional radially anisotropic model of shear velocity in the whole mantle, *Geophys. J. Int.*, **167**, 361–379.
- Park, J. & Levin, V., 2002. Seismic anisotropy: Tracing plate dynamics in the mantle, *Science*, **296**, 485–489.
- Plomerová, J. & Babuška, V., 2010. Long memory of mantle lithosphere fabric-European LAB constrained from seismic anisotropy, *Lithos*, **120**, 131–143.
- Plomerová, J., Munzarová, H., Vecsey, L., Kissling, E., Achauer, U. & Babuška, V., 2016. Cenozoic volcanism in the Bohemian Massif in the context of P-and S-velocity high-resolution teleseismic tomography of the upper mantle, *Geochem. Geophys. Geosyst.*, **17**(8), 3326–3349.
- Plomerová, J., Vecsey, L. & Babuška, V. & LAPNET working group, 2011. Domains of Archean mantle lithosphere deciphered by seismic anisotropy— inferences from the LAPNET array in northern Fennoscandia, *Solid Earth*, **2**, 303–313.
- Plomerová, J., Vecsey, L. & Babuška, V., 2012. Mapping seismic anisotropy of the lithospheric mantle beneath the northern and eastern Bohemian Massif (central Europe), *Tectonophysics*, **564–565**, 38–53.
- Raitt, R.W., Shor, G.G., Francis, T.J.G. & Morris, G.B., 1969. Anisotropy of the Pacific upper mantle, *J. Geophys. Res.*, **74**, 3095–9109.
- Sandoval, S., , 2002. , The Lithosphere-Asthenosphere System Beneath Fennoscandia (Baltic shield) by Body-Wave Tomography, *PhD thesis*, Swiss Federal Institute of Technology, Zürich, Switzerland.
- Sandoval, S., Kissling, E. & Ansorge, J. & SVEKALAPKO Seismic Tomography working Group, 2004. High-resolution body wave tomography beneath the SVEKALAPKO array - II. Anomalous upper mantle structure beneath the central Baltic Shield, *Geophys. J. Int.*, **157**, 200–214.
- Savage, M.K., 1999. Seismic anisotropy and mantle deformation: what have we learned from shear wave splitting? *Rev. Geophys.*, **37**, 65–106.
- Shomali, Z.H., Roberts, R.G. & Pedersen, L.B. & the TOR Working Group, 2006. Lithospheric structure of the Tornquist Zone resolved by nonlinear P and S teleseismic tomography along the TOR array, *Tectonophysics*, **416**, 133–149.
- Silvennoinen, H., Kozlovskaya, E. & Kissling, E., 2016. POLENET/LAPNET teleseismic P wave travel time tomography model of the upper mantle beneath northern Fennoscandia, *Solid Earth*, **7**, 425–439.
- Silver, P.G., 1996. Seismic anisotropy beneath the continents: probing the depths of geology, *Annu. Rev. Earth Planet. Sci.*, **24**, 385–432.
- Sobolev, S., Gresillaud, A. & Cara, M., 1999. How robust is isotropic delay time tomography for anisotropic mantle? *Geophys. Res. Lett.*, **26**(4), 509–512.
- Spakman, W., Van der Lee, S. & Van der Hilst, R., 1993. Travel-time tomography of the European-Mediterranean mantle down to 1400 km, *Phys. Earth planet. Inter.*, **79**, 3–74.
- Tian, Y. & Zhao, D., 2012. Seismic anisotropy and heterogeneity in the Alaska subduction zone, *Geophys. J. Int.*, **190**, 629–649.
- Tian, Y. & Zhao, D., 2013. Reactivation and mantle dynamics of North China Craton: insight from P-wave anisotropy tomography, *Geophys. J. Int.*, **195**, 1796–1810.
- Vecsey, L., Plomerová, J., Kozlovskaya, E. & Babuška, V., 2007. Shear-wave splitting as a diagnostic of varying upper mantle structure beneath south-eastern Fennoscandia, *Tectonophysics*, **438**, 57–77.
- Wang, J. & Zhao, D., 2008. P-wave anisotropic tomography beneath Northeast Japan, *Phys. Earth planet. Inter.*, **170**, 115–133.
- Wang, J. & Zhao, D., 2012. P wave anisotropic tomography of the Nankai subduction zone in Southwest Japan, *Geochem. Geophys. Geosyst.*, **13**, Q05017.
- Wang, J. & Zhao, D., 2013. P-wave tomography for 3-D radial and azimuthal anisotropy of Tohoku and Kyushu subduction zones, *Geophys. J. Int.*, **193**, 1166–1181.
- Weiland, C., Steck, L., Dawson, P. & Korneev, V., 1995. Nonlinear teleseismic tomography at Long Valley caldera, using three-dimensional minimum travel time ray tracing, *J. geophys. Res.*, **100**, 20379–20390.
- Wei, W., Zhao, D. & Xu, J., 2013. P-wave anisotropic tomography in Southeast Tibet: new insight into the lower crustal flow and seismotectonics, *Phys. Earth planet. Inter.*, **222**, 47–57.
- Wessel, P. & Smith, W.H.F., 1998. New, improved version of the generic mapping tools released, *EOS. Trans. Am. Geophys. Un.*, **79**, 579.
- Yuan, H., French, S., Cupillard, P. & Romanowicz, B., 2014. Lithospheric expression of geological units in central and eastern North America from full waveform tomography, *Earth planet. Sci. Lett.*, **402**, 176–186.
- Yu, D. & Wang, L., 2013. P-wave anisotropy tomography of central Japan: insight into subduction dynamics, *Tectonophysics*, **592**, 14–30.
- Zhu, H., Bozdağ, E. & Tromp, J., 2014. Seismic structure of the European upper mantle based on adjoint tomography, *Geophys. J. Int.*, **201**, 18–52.
- Šílený, J. & Plomerová, J., 1996. Inversion of shear-wave splitting parameters to retrieve three-dimensional orientation of anisotropy in continental lithosphere, *Phys. Earth planet. Inter.*, **95**, 277–292.

## SUPPORTING INFORMATION

Supplementary data are available at *GJI* online.

**Figure S1.** (a) Scheme of anisotropy with hexagonal symmetry with inclined high-velocity axis  $a$  or low-velocity axis  $b$ . Teleseismic  $P$  waves can hardly distinguish, due to their angles of incidence, between these two types of hexagonal symmetry. (b) Comparison of  $P$ -wave velocities calculated according to approximate eq. (5) in red and those evaluated as solution of the Christoffel equation, that is exact theoretical values, in black. The elastic coefficients chosen for this example correspond to a hexagonal model of peridotite aggregate (e.g. Ben Ismail & Mainprice 1998; Babuška & Plomerová 2006).

**Figure S2.** Resulting model parameters corresponding to perturbations of isotropic component of velocity for damping factors of 10 (a) and 100 (b), strength of anisotropy for damping factors of 100 (c) and 1000 (d) and inclination of the symmetry axis for damping factors of 0.5 (e) and 5 (f). Only one of the four damping factors is always changed and we keep the other three damping factors at their finally selected values during these inversions. Higher damping results in slower convergence towards the correct model parameters. See also caption of Fig. 3.

**Figure S3.** Diagonal elements of the resolution matrix for all model parameters of testing series I (Section 4). Resolution of the symmetry-axis orientation depends on strength of anisotropy. At nodes with no or low strength of anisotropy, it is irrelevant to look for axis orientation.

**Figure S4.** Resulting model parameters after four iterations of synthetic inversions with different initial orientations of the symmetry axis from 30 to 180 km depth. See caption of Fig. 2 for description of visualization of the anisotropic parameters.

**Figure S5.** Resulting model parameters after four iterations of synthetic inversions with different initial orientations of the symmetry axis imaged together in the combined output model. See caption of Fig. 11 for more details.

**Figure S6.** Model of anisotropic velocities resulting from coupled anisotropic–isotropic inversion of synthetic traveltimes calculated for  $P$  waves propagating through the isotropic part of structure imaged in Fig. 9. See caption of Fig. 11 for more details.

**Figure S7.** Model of anisotropic velocities resulting from coupled anisotropic–isotropic inversion of synthetic traveltimes calculated for  $P$  waves propagating through the anisotropic part of the structure imaged in Fig. 9. See caption of Fig. 11 for more details.

**Figure S8.** Model of isotropic velocities resulting from purely isotropic-velocity inversion of synthetic traveltimes calculated for  $P$  waves propagating through the anisotropic part of the synthetic structure imaged in Fig. 9. See caption of Fig. 11 for more details. See caption of Fig. 11 for more details.

**Figure S9.** Model of anisotropic velocities resulting from inversion for strength of anisotropy and orientation of symmetry axis of synthetic travel times calculated for  $P$  waves propagating through the anisotropic part of structure imaged in Fig. 9. The isotropic-velocity component is fixed during the inversion. See caption of Fig. 11 for more details.

Please note: Oxford University Press is not responsible for the content or functionality of any supporting materials supplied by the authors. Any queries (other than missing material) should be directed to the corresponding author for the paper.

## APPENDIX A

The following demonstration is based on Backus (1965), considering modifications according to our assumptions. The non-zero small variations  $\gamma_{ijkl}$  of elastic coefficients introduced in eq. (2) can be

expressed as

$$\begin{aligned}\gamma_{1111} &= \gamma_{2222} = \frac{1}{\rho} [A - (\lambda + 2\mu)], \\ \gamma_{3333} &= \frac{1}{\rho} [C - (\lambda + 2\mu)], \\ \gamma_{1122} &= \frac{1}{\rho} [(A - 2N) - \lambda], \\ \gamma_{1133} &= \gamma_{2233} = \frac{1}{\rho} (F - \lambda), \\ \gamma_{1313} &= \gamma_{2323} = \frac{1}{\rho} (L - \mu), \\ \gamma_{1212} &= \frac{1}{2} (\gamma_{1111} - \gamma_{1122}) = \frac{1}{\rho} (N - \mu),\end{aligned}\quad (A1)$$

for a hexagonal anisotropy described by five independent elastic coefficients  $A$ ,  $C$ ,  $F$ ,  $N$  and  $L$  and for a background isotropic medium represented by Lamé constants  $\lambda$  and  $\mu$ .

The component of unit propagation vector  $\mathbf{n}$  parallel to the symmetry axis is  $n_3 = \cos \alpha$  and the component within plane ( $n_1$ ,  $n_2$ ) perpendicular to the symmetry axis equals  $\sin \alpha$ . Then, we have relation  $n_i n_i = 1$ . Furthermore, inserting coefficients  $\gamma_{ijkl}$  into eq. (2), we obtain

$$\begin{aligned}B^{(1)} &= \gamma_{1111} + 2(\gamma_{1133} + 2\gamma_{1313} - \gamma_{1111}) \cos^2 \alpha \\ &\quad + (\gamma_{1111} + \gamma_{3333} - 2\gamma_{1133} - 4\gamma_{1313}) \cos^4 \alpha.\end{aligned}\quad (A2)$$

Formula (A2) can be rewritten without any approximations as a finite Fourier series

$$B^{(1)} = P + Q \cos 2\alpha + R \cos 4\alpha,\quad (A3)$$

where the coefficients are

$$P = \frac{1}{8\rho} [3(A + C) + 2(F + 2L)] - \frac{\lambda + 2\mu}{\rho},\quad (A4)$$

$$Q = \frac{1}{2\rho} (C - A),\quad (A5)$$

$$R = \frac{1}{8\rho} [A + C - 2(F + 2L)].\quad (A6)$$

Then, anisotropic velocity (1) is expressed as

$$v = c + \frac{P}{2c} + \frac{Q}{2c} \cos 2\alpha + \frac{R}{2c} \cos 4\alpha.\quad (A7)$$

The  $\cos 4\alpha$  term is small in comparison with the  $\cos 2\alpha$  term in the upper mantle, which is supported by observations of variations of  $P_n$  velocity with azimuth (e.g. Raitt *et al.* 1969). Also our evaluation of coefficients  $Q$  and  $R$  for elastic constants of hexagonal-symmetry approximation of originally orthorhombic aggregate of peridotite (Ben Ismail & Mainprice 1998; Babuška & Plomerová 2006) results in ten times smaller  $R$  than  $Q$ . Thus we neglect the  $\cos 4\alpha$  term

$$v = c + \frac{P}{2c} + \frac{Q}{2c} \cos 2\alpha.\quad (A8)$$

The anisotropic velocity can in general be separated into a sum of isotropic ( $\bar{v}$ ) and directional ( $\delta v$ ) components

$$v = \bar{v} + \delta v.\quad (A9)$$

Comparing (A8) and (A9), it is obvious that

$$\bar{v} = c + \frac{P}{2c},\quad (A10)$$

$$\delta v = \frac{Q}{2c} \cos 2\alpha.\quad (A11)$$

Raising eq. (A10) to second power, combining it with (A4) and neglecting the  $P^2$  term as  $P \ll c^2$ , we get a relation for  $\bar{v}^2$

$$\bar{v}^2 = \frac{1}{8\rho} [3(A + C) + 2(F + 2L)].\quad (A12)$$

Strength of anisotropy commonly defined as

$$k = \frac{v^{\max} - v^{\min}}{\bar{v}} \quad (\text{A13})$$

can in our specific case be expressed as

$$k = \frac{4(C - A)}{3(A + C) + 2(F + 2L)} \quad (\text{A14})$$

taking into account the form of directional component (A11) of the  $P$ -wave velocity, substituting  $c$  for  $\bar{v}$  in the denominator as  $P << c^2$  and  $Q << c^2$  and including eqs (A5) and (A12).

Thus we may write the anisotropic velocity (A8) with the use of isotropic component of velocity (A12) and strength of anisotropy

(A14) as

$$v = \bar{v} + \frac{\bar{v}k}{2} \cos 2\alpha. \quad (\text{A15})$$

## APPENDIX B

Ray density tensor is a tool for assessment of resolution possibilities of a designed tomographic model parameterization along with particular ray geometry (Kissling 1988; Sandoval 2002; Sandoval *et al.* 2004). In addition to the hit-count, the ray density tensor takes into account the length of the ray paths through the cell (similarly as derivative weighted sum) and the ray orientations. To link ray coverage of a cell to a tensor is advantageous since a symmetric tensor can be easily represented by an ellipsoid (Fig. B1), length and orientation of semi-axes of which are defined by tensor eigenvalues and eigenvectors. In the ideal case of the cell being covered equally by the rays from all directions, the ray density tensor becomes an identity tensor and the ellipsoid turns into a sphere. On the other hand, an elongated ellipsoid denotes a direction, along which the rays prevailingly propagate through the cell. To assess the shape of an ellipsoid, it is not even necessary to visualize it. Comparison of the three eigenvalues provides us with the required information about ray coverage quality as well.

How can we transform the geometry of the ray paths within a cell into a tensor?

The part of the  $i$ th ray pertaining to the  $j$ th cell can be represented by vector  $\mathbf{a}_{ij}$  oriented along the ray direction within the cell. Length  $a_{ij}$  of the  $\mathbf{a}_{ij}$  vector is proportional to length  $l_{ij}$  of the ray part normalized by space diagonal  $L_j$  of the cell and the vector length may also depend on weight  $\omega_i$  assigned to the  $i$ th arrival time measurement (Sandoval 2002)

$$a_{ij} = \frac{l_{ij}}{L_j} \omega_i. \quad (\text{B1})$$

In a local coordinate system of the  $i$ th ray, such that unit vector  $\mathbf{x}^{\text{loc}}$  parallels the ray within the  $j$ th cell, and using 3x3 tensor notation,  $\mathbf{a}_{ij}$  gets the form

$$[\mathbf{a}_{ij}^{\text{loc}}] = \begin{pmatrix} a_{ij} & 0 & 0 \\ 0 & 0 & 0 \\ 0 & 0 & 0 \end{pmatrix}. \quad (\text{B2})$$

The square brackets and the italics symbolize that the variable is a 2-D array. Transforming  $[\mathbf{a}_{ij}^{\text{loc}}]$  from its local coordinate system to a global coordinate system and summing  $[\mathbf{a}_{ij}^{\text{glob}}]$  of all the rays crossing the  $j$ th cell, ray density tensor  $[\mathbf{RDT}_j]$  of the  $j$ th cell is obtained

$$[\mathbf{RDT}_j] = \sum_{i=1}^{n_{\text{rays}}} [\mathbf{a}_{ij}^{\text{glob}}]. \quad (\text{B3})$$

The relation between the local and global coordinate systems is given by orientation of the ray, which is in our case described by the event backazimuth  $\phi$  and ray incidence angle  $i$  (Fig. B2).

The transformation of the coordinates of  $[\mathbf{a}_{ij}]$  from its local to the global coordinate system is according to the tensor transformation law performed as

$$[\mathbf{a}_{ij}^{\text{glob}}] = [\mathbf{T}] [\mathbf{a}_{ij}^{\text{loc}}] [\mathbf{T}]^T, \quad (\text{B4})$$

where  $[\mathbf{T}]$  is the transformation matrix and  $[\mathbf{T}]^T$  is  $[\mathbf{T}]$  transposed.

To derive the transformation matrix for our case, the inverse transformation, that is from the global to the local coordinate system

$$[\mathbf{a}_{ij}^{\text{loc}}] = [\mathbf{T}]^T [\mathbf{a}_{ij}^{\text{glob}}] [\mathbf{T}], \quad (\text{B5})$$

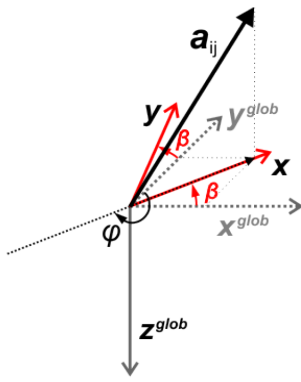


**Figure B3.** Coordinate system rotated about  $\mathbf{z}$ -axis by angle  $\beta$  so that  $\mathbf{x}$ -axis parallels the ray part azimuth.  $\phi$  is event back-azimuth. See eq. (B6) for relation between rotation angle  $\beta$  and event back-azimuth  $\phi$ .

is more illustrative because the aim of such a transformation is to orient the  $\mathbf{x}$ -axis to become parallel with  $\mathbf{a}_{ij}$  in the local coordinate system while  $\mathbf{y}$ - and  $\mathbf{z}$ -axes might be oriented arbitrarily. The transformation of the coordinate system from global to local can be reached by two subsequent rotations (always one axis fixed). First transformation  $[\mathbf{T}_1]$  of the global coordinate system is a rotation about  $\mathbf{z}$ -axis by angle  $\beta$  (from  $\mathbf{x}$  to  $\mathbf{y}$ ) to align  $\mathbf{x}$  with the azimuth of  $\mathbf{a}_{ij}$  (Fig. B3). In terms of event backazimuth  $\phi$ , rotation angle  $\beta$  can

be expressed as

$$\beta = \frac{\pi}{2} - (\phi - \pi) = \frac{3\pi}{2} - \phi. \quad (\text{B6})$$

Transformation matrix  $[\mathbf{T}_1]$  is then written as

$$[\mathbf{T}_1] = \begin{pmatrix} \cos \beta & \sin \beta & 0 \\ -\sin \beta & \cos \beta & 0 \\ 0 & 0 & 1 \end{pmatrix} = \begin{pmatrix} -\sin \phi & -\cos \phi & 0 \\ \cos \phi & -\sin \phi & 0 \\ 0 & 0 & 1 \end{pmatrix}. \quad (\text{B7})$$

The second transformation  $[\mathbf{T}_2]$  is a rotation about  $\mathbf{y}$ -axis by angle  $\gamma$  (from  $\mathbf{z}$  to  $\mathbf{x}$ ) to tilt  $\mathbf{x}$  up to make it parallel with  $\mathbf{a}_{ij}$  (Fig. B4). Expressing  $\gamma$  by ray incidence angle  $i$ , we obtain

$$\gamma = \frac{\pi}{2} - i. \quad (\text{B8})$$

And transformation matrix  $[\mathbf{T}_2]$  can be expressed as

$$[\mathbf{T}_2] = \begin{pmatrix} \cos \gamma & 0 & -\sin \gamma \\ 0 & 1 & 0 \\ \sin \gamma & 0 & \cos \gamma \end{pmatrix} = \begin{pmatrix} \sin i & 0 & -\cos i \\ 0 & 1 & 0 \\ \cos i & 0 & \sin i \end{pmatrix}. \quad (\text{B9})$$

The transformation of  $\mathbf{a}_{ij}$  from the global coordinate system into the local one is then

$$[\mathbf{a}_{ij}^{loc}] = [\mathbf{T}_2][\mathbf{T}_1][\mathbf{a}_{ij}^{glob}][\mathbf{T}_1]^T[\mathbf{T}_2]^T \quad (\text{B10})$$

and the inverse transformation

$$[\mathbf{a}_{ij}^{glob}] = [\mathbf{T}_1]^T[\mathbf{T}_2]^T[\mathbf{a}_{ij}^{loc}][\mathbf{T}_2][\mathbf{T}_1]. \quad (\text{B11})$$

Inserting eqs (B2), (B7) and (B9) into formula (B11), we obtain

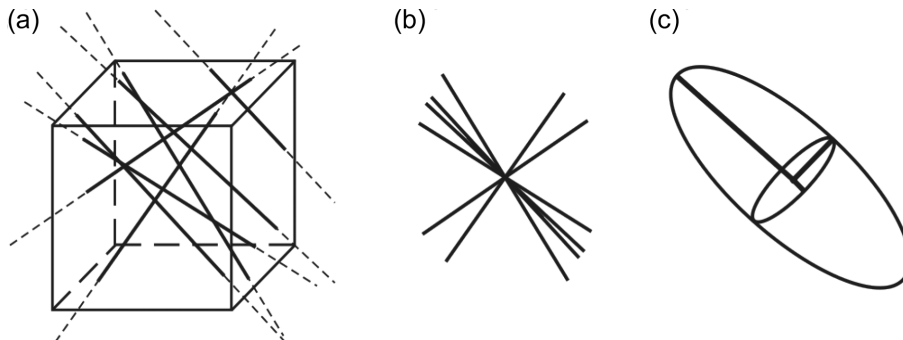


**Figure B1.** Generation of ray density tensor, after Kissling (1988). (a) Rays crossing a cell of a tomographic model parametrization. (b) Centred ray parts. (c) Ellipsoid best approximating the distribution of the ray parts within the cell.

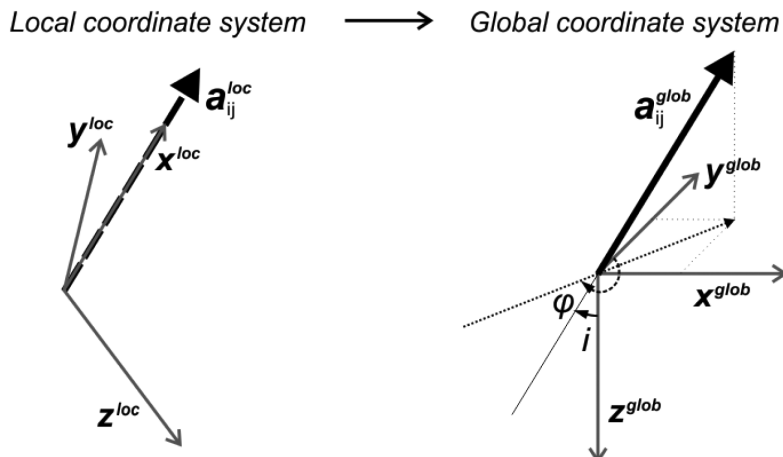


**Figure B2.** In the coordinate system of the ray part, that is in the local coordinate system,  $\mathbf{x}$ -axis parallels the ray propagation direction represented by vector  $\mathbf{a}_{ij}$ . In the global coordinate system, each ray part is defined by its incidence angle  $i$  and event backazimuth  $\phi$ .

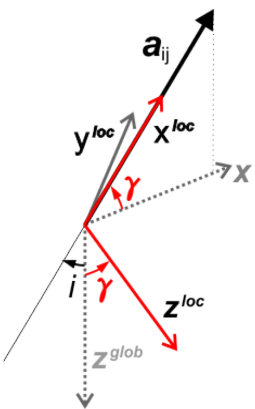


**Figure B4.** Coordinate system rotated about  $y$ -axis by angle  $\gamma$  so that  $x$ -axis points towards the ray propagation.  $i$  is ray incidence angle. See eq. (B8) for relation between rotation angle  $\gamma$  and incidence angle  $i$ .

the relation for tensor  $[a_{ij}^{glob}]$

$$[a_{ij}^{glob}] = a_{ij} \begin{pmatrix} \sin^2 i \sin^2 \phi & \sin^2 i \sin \phi \cos \phi & \sin i \cos i \sin \phi \\ \sin^2 i \sin \phi \cos \phi & \sin^2 i \cos^2 \phi & \sin i \cos i \cos \phi \\ \sin i \cos i \sin \phi & \sin i \cos i \cos \phi & \cos^2 i \end{pmatrix}. \quad (\text{B12})$$

Summation of eq. (B12) for all rays crossing the  $j$ th cell results in ray density tensor (eq. B3). The ray density tensor is obviously symmetric.